J. Mech. Phys. Solids 181 (2023) 105453

Contents lists available at ScienceDirect

Journal of the Mechanics and Physics of Solids

journal homepage: www.elsevier.com/locate/jmps

Data-driven hyperelasticity, Part II: A canonical framework for anisotropic soft biological tissues

Oğuz Ziya Tikenoğulları [a,b,1], Alp Kağan Açan [a,c,1], Ellen Kuhl [b], Hüsnü Dal [a,c,*]

[a] Department of Mechanical Engineering, Middle East Technical University, Ankara, Turkey
[b] Department of Mechanical Engineering, Stanford University, Stanford CA, United States of America
[c] Computational Micromechanics Laboratory, CAD/CAM Robotics Center, Middle East Technical University, Ankara, Turkey

ARTICLE INFO

Keywords:
Data-driven modeling
Hyperelasticity
Anisotropy
Soft biological tissues
Fiber dispersion
Von Mises distribution

ABSTRACT

In this work, we present a novel anisotropic data-driven hyperelasticity framework for the constitutive modeling of soft biological tissues that allows direct incorporation of experimental data into the constitutive model, without requirement of a predetermined mathematical formula for the strain–energy density function. The data-driven framework is constructed through a dispersion-type anisotropic formulation based on a generalized structure tensor in the sense of Holzapfel et al. (2015) that take into account in- and out of plane dispersion. The partial derivatives of the strain energy density functions are replaced with appropriate B-spline interpolations where the control points are calibrated against experimental data obtained from uniaxial tension, triaxial shear, and (equi)biaxial tension deformations. The model calibration phase incorporates the normalization condition and the polyconvexity condition is enforced through the control points of the B-splines in order to ensure a stable constitutive response that allows unique solution in finite element analysis. The predictive capabilities of the proposed model are shown against linea alba, rectus sheath, aneurysmal abdominal aorta, and myocardium tissues. On the numerical side, the stress and moduli expressions of the model are derived and implemented into the finite element method. The performance of the model is demonstrated through representative boundary value problems.

1. Introduction

Soft biological tissues, such as muscle, skin, and cartilage play important roles in the human body and have unique mechanical properties that are essential for proper functioning. Significant effort has been devoted to the constitutive modeling of biological soft tissues in the last decades, with a focus on understanding their mechanical behavior, which is crucial in developing treatments and therapies that rely on mechanobiological functions. Soft biological tissues exhibit a highly non-linear mechanical response under large deformations. The literature abounds with endeavors to capture the non-linear mechanical behavior of biological soft tissues, which can be broadly classified into two categories: approaches that assume perfectly aligned fibers, and (ii) approaches that consider fiber dispersion. Tong and Fung (1976) proposed a hyperelastic free energy function in terms of Green–Lagrange strain components, and this approach was further developed in subsequent works by Fung et al. (1979), Chuong and Fung (1983), and Humphrey (1995). Various free energy function in terms of the invariants of the right Cauchy–Green tensor have been proposed in e.g. polynomial (Horgan and Saccomandi, 2005; Humphrey et al., 1990; Murphy, 2013), power (Balzani et al., 2006; Ghaemi

* Corresponding author at: Department of Mechanical Engineering, Middle East Technical University, Ankara, Turkey.
E-mail address: dal@metu.edu.tr (H. Dal).

1 Contributed equally to this manuscript.

https://doi.org/10.1016/j.jmps.2023.105453
Received 7 July 2023; Received in revised form 22 September 2023; Accepted 1 October 2023
Available online 9 October 2023
0022-5096/

et al., 2009), and exponential (Holzapfel et al., 2000, 2005; May-Newman and Yin, 1998; Weiss et al., 1996) functional forms, respectively. However, these models assume that fibers are perfectly aligned. There is a number of morphological studies on animal or human samples that address fiber dispersion in the biological soft tissues (Karlon et al., 1998; Schriefl et al., 2012b, 2013, 2012c; Sommer et al., 2015; Strijkers et al., 2009; Usyk et al., 2001). To address this issue, Lanir (1979) proposed a framework for modeling flat biological tissues using an angular integration approach that considers the dispersion of collagen and elastin fibers. The angular integration-type fiber dispersion approach has been further elaborated by Alastrué et al. (2009, 2010), Billiar and Sacks (2000), Driessen et al. (2005), Sacks (2003), Zulliger et al. (2004). Alternative approach to account for fiber dispersion is the use of a *generalized structure tensor* (GST) in the sense of Gasser et al. (2006) that uses a single dispersion parameter motivated by a planar von Mises density distribution function. This model was later extended by Holzapfel et al. (2015) to include out-of-plane dispersion of fibers in terms of two scalar dispersion parameters based on a bivariate von Mises distribution. For more information, we refer to the comprehensive reviews (Fung, 1993; Humphrey, 1995, 2002; Gasser et al., 2006; Chagnon et al., 2015; Mihai et al., 2015; Kalra et al., 2016; Holzapfel et al., 2019; Bhattarai et al., 2021; Dal et al., 2023a) *inter alia*. In recent years, data-driven constitutive modeling has emerged as a promising approach in computational solid mechanics and it may trigger *a new paradigm* for constitutive modeling of biological soft tissues. The data-driven approaches can be classified into two main groups; (i) distance-minimization approach, (ii) explicit data-driven approaches. The distance-minimization approach was developed by Kirchdoerfer and Ortiz (2016). In classical constitutive modeling or explicit data-driven modeling, the material data is used in computation by means of material parameters. However, in the approach of Kirchdoerfer and Ortiz (2016), the material data is directly used inside the computation. They reformulated the classical boundary value problem by means of distances between states in the constraint and material set. The constraint set involves fundamental balance equations and the problem's boundary conditions whereas the material data set includes the admissible material states. The aim of the distance-minimization the approach is to find the state in the constraint set which is closest to the material data set by using an iterative solver. Kirchdoerfer and Ortiz (2016) initially applied their approach to linear-elastic truss system, then extended the work to the dynamic application by using Newmark framework (Kirchdoerfer and Ortiz, 2018). We also refer to Ibanez et al. (2017) for a similar treatment. Later on, the distance-minimization approach was extended to finite strains (Conti et al., 2020; Nguyen and Keip, 2018; Nguyen et al., 2020; Platzer et al., 2019). In this context, local search algorithms (Kanno, 2018b), statistical learning based on kernel regression (Kanno, 2018a), or accelerated distance minimization techniques grounded on smooth tangent operators for the hidden material manifold (Nguyen et al., 2022) have been recently proposed. Ibanez et al. (2018) and Eggersmann et al. (2019) extended the distance-minimization approach to inelasticity. The distance-minimization approach is a completely model-free approach and requires new data-driven solvers; whereas spline-based and neural-network-based approaches can be easily implemented into classical finite element solvers. On the other hand, in explicit data-driven approaches, the material data does not appear in computation directly; however, the material data can be reduced to a set of variables depending on the employed technique, i.e., the weights in the neural network approaches, or control points in the spline-based approaches. The use of data-driven constitutive modeling using neural networks began with Ghaboussi et al. (1991), who trained a neural network on experimental data. This was followed by the work of Lefik and Schrefler (2003), who proposed a new non-linear neural network model for elastoplastic materials. Hashash et al. (2004) conducted the first study in which consistent tangent moduli were derived and a neural network model was implemented into a finite element simulation. However, prior to this, neural network-based models did not prioritize thermodynamic considerations or convexity. More recently, Xu et al. (2021) and Linka et al. (2021) introduced constitutive neural network models that consider energy functional convexity, and Linka and Kuhl (2023) and Tac et al. (2022) proposed polyconvex neural network models to model anisotropic materials. An alternative approach to data-driven modeling using neural networks is spline interpolation, which was first proposed by Sussman and Bathe (2009) using cubic splines based on logarithmic strains to interpolate experimental data points for isotropic materials. This approach has since been extended to transversely isotropic and orthotropic materials (Latorre and Montáns, 2013, 2014). In the first part (Dal et al., 2023b), we have proposed a canonical representation of isotropic hyperelasticity based on (i) principal stretches, (ii) principal invariants, and (iii) modified invariants and proposed convenient algorithmic treatment for the finite element method. Most of the existing constitutive models for soft biological tissues were proposed and calibrated for a particular tissue. The microstructure of different tissue types, such as arterial wall, abdominal muscle, myocardium, or connective tissues and corresponding macro-mechanical response can vary significantly. Such variation can be either due to distribution of collagen fibers or due to the organization and interaction the constituents tissue, namely the elastin and collagen. Aging also plays an important role on the tissue architecture and alters the mechanical response significantly. In this regard, exponential, power, logarithmic, polynomial forms of functions for the stress expressions, which are appropriate for specific-type of tissues have been proposed, see e.g. Ateshian et al. (2009), Holzapfel et al. (2000), Ogden and Saccomandi (2007) among others. Although the dispersion-type anisotropic formulations provide a more flexible representation for the degree and distribution of anisotropy, a particular constitutive model developed for one type of tissue may not accurately capture the mechanical response of another tissue (Dal et al., 2023a). This motivates an alternative approach, *the data-driven constitutive modeling* as a *new paradigm* in computational biomechanics: Within this context, this work aims to develop a generalized framework for data-driven anisotropic hyperelasticity, a single computational framework that can model all existing biological tissues. For the anisotropic response, we take into account the dispersion of fibers in terms of a generalized structure tensor in the sense of Gasser et al. (2006) and Holzapfel et al. (2015) where the dispersion is controlled by single/two material parameters along with a mean fiber orientation direction, respectively. The free energy function is further decomposed into isotropic and anisotropic parts. Rather than assuming an analytical form for the free energy function, we interpolate the derivatives of the free energy function in terms of B-spline functions which are calibrated from experimental datasets. The algorithmic treatment of the data-driven framework for the finite element method is presented. The model is implemented into the general-purpose finite element analysis program Feap (Taylor, 2014) and the efficiency of the data-driven framework is

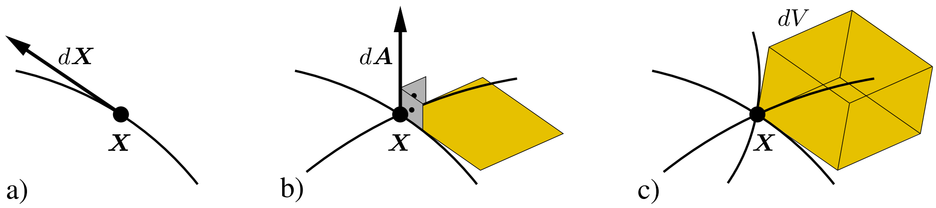

Fig. 1. Three fundamental maps of a continuum: (a) The deformation gradient $\boldsymbol{F}$ as a mapping of an infinitesimal line element, (b) its cofactor $\operatorname{cof}[\boldsymbol{F}]$ as an area map, and (c) and its determinant $\det[\boldsymbol{F}]$ as a volume map.

demonstrated via representative boundary value problems. The paper is organized as follows: Section 2 outlines the fundamentals of the dispersion-based anisotropic hyperelastic solids. In Section 3, the proposed data-driven approach along with theory of B-splines is presented. Moreover, basic requirements for material theory such as material objectivity, dissipation inequality, polyconvexity, and growth conditions are discussed. In Section 4, we demonstrate the performance of the anisotropic data-driven constitutive framework with respect to experimental results obtained from myocardium, abdominal aortic aneurysm tissue, linea alba, rectus sheath and myocardium, respectively. In Section 5, the model performance at structural level is demonstrated through a boundary value problem. Finally, the manuscript closes with concluding remarks in Section 6.

2. Kinematics of hyperelastic deformable solids

In this section, kinematics, fiber dispersion modeling in the sense of structure tensors, and stress expressions for an anisotropic hyperelastic continuum will be introduced and the corresponding mathematical framework will be briefly discussed.

2.1. Basic maps

Let the deformation map $\boldsymbol{\varphi}(\boldsymbol{X}, t)$ represent the motion of a deformable solid body. It maps the reference/Lagrangian configuration of a material point $\boldsymbol{X} \in \mathscr{B}_0$ onto the current/Eulerian configuration of material points $\boldsymbol{x} = \boldsymbol{\varphi}_t(\boldsymbol{X})$ at time $t \in \mathscr{T} \subset \mathbb{R}_+$. The *deformation gradient*

$$\boldsymbol{F} : T_X\mathscr{B}_0 \to T_x\mathscr{B}; \quad \boldsymbol{F} := \frac{\partial \boldsymbol{\varphi}_t(\boldsymbol{X})}{\partial \boldsymbol{X}} \tag{1}$$

maps a unit tangent vector of the reference configuration onto its counterpart in the current configuration, where $T_X\mathscr{B}_0$ and $T_x\mathscr{B}$ denote the tangent spaces in the reference and current configurations, respectively. Additionally, the co-tangent spaces in the reference and current manifolds are represented as $T^*_X\mathscr{B}_0$ and $T^*_x\mathscr{B}$, respectively. The locally furnished coordinate systems for the reference and spatial configurations are generally non-orthogonal but equipped with the covariant reference metric $\boldsymbol{G}$ and the spatial metric $\boldsymbol{g}$, required for the mapping between the co- and contra-variant objects in the Lagrangian and Eulerian manifolds. In the Cartesian basis system, the metric tensors $\boldsymbol{G} = \delta_{AB}$, $\boldsymbol{g} = \delta_{ab}$ simply reduce to Kronecker delta and are merely used for index raising and lowering procedures. The normal map between the unit normals in the reference and current configurations is defined as

$$\boldsymbol{F}^{-T} : T^*_X\mathscr{B}_0 \to T^*_x\mathscr{B}. \tag{2}$$

In this sequence, let line, area, and volume elements in the Lagrangian configurations are denoted as $d\boldsymbol{X}$, $d\boldsymbol{A}$, and dV, respectively. The Eulerian counterparts of these elements are obtained through the deformation gradient $\boldsymbol{F}$, its cofactor $\operatorname{cof}[\boldsymbol{F}] = \det[\boldsymbol{F}]\boldsymbol{F}^{-T}$ and its Jacobian $\det[\boldsymbol{F}]$

$$d\boldsymbol{x} = \boldsymbol{F}d\boldsymbol{X}\ , \qquad d\boldsymbol{a} = \operatorname{cof}[\boldsymbol{F}]d\boldsymbol{A}\ , \qquad dv = \det[\boldsymbol{F}]\,dV, \tag{3}$$

see also Fig. 1. $J = \det \boldsymbol{F} > 0$ guarantees non-penetrable deformations $\boldsymbol{\varphi}_t(\boldsymbol{X})$.

2.2. Deformation measures

The *right Cauchy–Green tensor* is defined as

$$\boldsymbol{C} = \boldsymbol{F}^T\boldsymbol{g}\boldsymbol{F} \quad \text{with} \quad C_{AB} = F^a{}_A g_{ab} F^b{}_B \tag{4}$$

the pull-back of the current metric $\boldsymbol{g}$ to the reference configuration. In this context, it is common practice to split the deformation gradient $\boldsymbol{F}$ into dilatational and volume-preserving parts

$$\boldsymbol{F} = \boldsymbol{F}_{\text{vol}}\bar{\boldsymbol{F}} \quad \text{with} \quad \boldsymbol{F}_{\text{vol}} := J^{1/3}\mathbf{1}. \tag{5}$$

The corresponding deformation measure reads

$$\boldsymbol{C} = J^{2/3}\bar{\boldsymbol{C}} \quad \text{with} \quad \bar{\boldsymbol{C}} = \bar{\boldsymbol{F}}^T\boldsymbol{g}\bar{\boldsymbol{F}}. \tag{6}$$

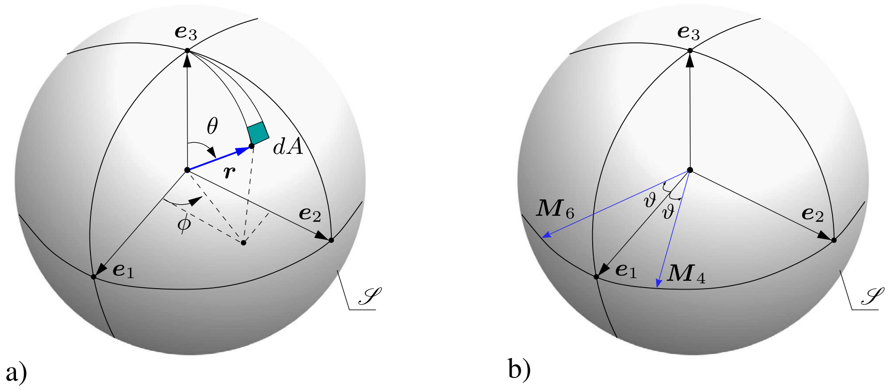

Fig. 2. (a) The unit micro-sphere and the orientation vector, (b) mean fiber directions of two families of fiber lie on $\boldsymbol{e}_1 - \boldsymbol{e}_2$ plane.

Two isotropic invariants of the right Cauchy–Green tensor are

$$\bar{I}_1 := \mathrm{tr}_{\boldsymbol{G}^{-1}}[\bar{\boldsymbol{C}}] = \bar{\boldsymbol{C}} : \boldsymbol{G}^{-1}, \qquad \text{and} \qquad I_3 := J^2 = \det[\boldsymbol{C}]. \tag{7}$$

For an infinitesimal cubic element, the three isotropic invariants of the right Cauchy–Green stretch tensor are associated with *linear*, *areal*, and *volumetric* stretches in the principal directions.

Here we define the derivatives of the invariants with respect to the right Cauchy–Green tensor $\boldsymbol{C}$ and its volume-conserving counterpart $\bar{\boldsymbol{C}}$, as they appear in the calculation of stress tensors,

$$\partial_{\bar{\boldsymbol{C}}} \bar{I}_1 = \boldsymbol{G}^{-1} \qquad \partial_{\boldsymbol{C}} J = \tfrac{1}{2} J \boldsymbol{C}^{-1}. \tag{8}$$

2.3. Dispersion-type anisotropy: Generalized structure tensor

In dispersion-type anisotropic formulation, biological tissue is considered a fiber-reinforced composite with the fibers distributed in an isotropic matrix. Models developed within this framework are capable of accurately describing the effect of the structural arrangement of the fibers on the mechanical response. Dispersion-type anisotropic approaches utilize density distribution functions to represent the distributed fiber architecture of tissues. Let unit fiber direction $\boldsymbol{r}$ on a unit-sphere be given in the undeformed configuration. The fiber density in direction $\boldsymbol{r}$ is expressed with $\rho(\boldsymbol{r})$. The generalized structure tensor is defined as

$$\boldsymbol{H} = \frac{1}{|\mathscr{S}|} \int_{\mathscr{S}} \rho(\boldsymbol{r}) \boldsymbol{r} \otimes \boldsymbol{r} \; dA \quad \text{with} \quad \mathrm{tr}_{\boldsymbol{G}^{-1}} \boldsymbol{H} = 1, \tag{9}$$

where $\mathscr{S}$ represents the surface of a unit sphere and $\mathscr{S} = 4\pi$ for a unit sphere. It is possible to assume a distribution profile as an ansatz for $\rho(r)$ and find parameters of this ansatz function by fitting to the histologic observation of the fibrous tissue. Here we consider two different generalized structure tensor representations using planar and bi-variate von Mises distribution assumptions.

Planar von Mises distribution: Formulation of the generalized structure tensor employing a von Mises distribution function was proposed in Gasser et al. (2006) for arterial tissue. Here, a rotationally symmetric distribution is assumed around the mean fiber direction, which is then chosen to coincide with $\boldsymbol{e}_3$, without loss of generality. It follows that the distribution $\rho(\boldsymbol{r})$ becomes a function of θ only (see Fig. 2a). This model was later employed to model dispersion in myocardial tissue (Eriksson et al., 2013; Gültekin et al., 2016; Sommer et al., 2015). Two dispersion parameters κ_f, κ_s arise for two fiber families that we index with f and s standing for fiber and sheet directions. Evaluating the Eq. (9) for this specific choice of distribution profile, the generalized structure tensor attains the form

$$\boldsymbol{H}_f = \kappa_f \boldsymbol{1} + (1 - 3\kappa_f) \boldsymbol{f}_0 \otimes \boldsymbol{f}_0 \quad \text{and} \quad \boldsymbol{H}_s = \kappa_s \boldsymbol{1} + (1 - 3\kappa_s) \boldsymbol{s}_0 \otimes \boldsymbol{s}_0 \,, \tag{10}$$

for two fiber families that have the mean fiber directions $\boldsymbol{f}_0$ and $\boldsymbol{s}_0$ in the reference configuration. Some constitutive models for myocardium account for anisotropic shear stress contribution through the shearing between two fiber families using an additional structural tensor

$$\boldsymbol{H}_{fs} = (\boldsymbol{f}_0 \otimes \boldsymbol{s}_0)^{\mathrm{sym}} \,. \tag{11}$$

Resulting anisotropic invariants accounting for fiber dispersion and its derivative are,

$$E_i := \boldsymbol{H}_i : \bar{\boldsymbol{C}} \quad \text{and} \quad \partial_{\bar{\boldsymbol{C}}} E_i = \boldsymbol{H}_i \,, \quad \text{for} \quad i = \{f, s, fs\} \,. \tag{12}$$

The Eulerian counterparts of the generalized structure tensors read

$$\boldsymbol{h}_f = \kappa_f \boldsymbol{b} + (1 - 3\kappa_f) \boldsymbol{f} \otimes \boldsymbol{f}, \quad \boldsymbol{h}_s = \kappa_s \boldsymbol{b} + (1 - 3\kappa_s) \boldsymbol{s} \otimes \boldsymbol{s}, \quad \text{and} \quad \boldsymbol{h}_{fs} = (\boldsymbol{f} \otimes \boldsymbol{s})^{\mathrm{sym}} \,. \tag{13}$$

The Eulerian description of (12)$_1$ and its derivative can be expressed as

$$E_i := \boldsymbol{h}_i : \boldsymbol{g} \quad \text{and} \quad \partial_{\boldsymbol{g}} E_i = \boldsymbol{h}_i\,, \quad \text{for} \quad i = \{f, s, fs\}\,. \tag{14}$$

Bivariate von Mises distribution: Holzapfel et al. (2015) proposed a bivariate von Mises distribution function as an ansatz for $\rho(\boldsymbol{r})$ in Eq. (9), as a generalization of the planar Von Mises distribution to a three-dimensional distribution that takes into account in- and out-of-plane dispersion of collagen fibers. The bivariate dispersion model is motivated by the histology data collected from intima, media, and adventitia of human non-atherosclerotic thoracic abdominal aortas and common iliac arteries (Schriefl et al., 2012c). As the data suggests, this model assumes in-plane and out-of-plane symmetries such that $\rho(\theta,\phi) = \rho(\theta+\pi,\phi)$ and $\rho(\theta,\phi) = \rho(\theta,-\phi)$. In addition, mean fiber directions of two fiber families are assumed to lie in the $\boldsymbol{e}_1 - \boldsymbol{e}_2$ plane, symmetric around the $\boldsymbol{e}_2$ direction, separated with an angle of 2ϑ (see, Fig. 2b).

The bi-variate dispersion model was fitted to the experimental data collected from abdominal aorta tissue samples in Niestrawska et al. (2016), in order to compare dispersion characteristics between healthy and aneurismatic tissues. Generalized structure tensors for fiber families 4 and 6 read

$$\boldsymbol{H}_i = A\boldsymbol{1} + B\boldsymbol{M}_i \otimes \boldsymbol{M}_i + (1 - 3A - B)\boldsymbol{M}_n \otimes \boldsymbol{M}_n\,, \quad \text{for} \quad i = \{4, 6\}\,, \tag{15}$$

where $\boldsymbol{M}_i$, $i = \{4,6\}$ are the mean fiber directions shown in Fig. 2b and $\boldsymbol{M}_n$ is the out-of-plane vector that coincides with $\boldsymbol{e}_3$ in local material coordinate system. $A = 2\kappa_{ip}\kappa_{op}$ and $B = 2\kappa_{op}(1 - 2\kappa_{ip})$ are found from the experimental data of tissue histology. Herein, the mean fiber stretch and its derivative can be described as

$$E_i := \boldsymbol{H}_i : \bar{\boldsymbol{C}} \quad \text{and} \quad \partial_{\bar{\boldsymbol{C}}} E_i = \boldsymbol{H}_i \quad \text{for} \quad i = \{4, 6\}\,. \tag{16}$$

2.4. Free-energy function and the Lagrangian/Eulerian stress expressions

Hyperelastic mechanical behavior can be described using the Helmholtz free-energy function that represents the stored energy resulting from mechanical deformation. Polymeric materials and soft biological tissues exhibit a distinct response to bulk deformation and shear-type deformations. Based on Eqs. (5) and (6), the Lagrangian and Eulerian representations of the free-energy function can expressed as

$$\Psi(\boldsymbol{C}, \boldsymbol{H}_i) = U(J) + \bar{\Psi}(\bar{\boldsymbol{C}}, \boldsymbol{H}_i) \quad \text{and} \quad \Psi(\boldsymbol{g}; \boldsymbol{F}, \boldsymbol{H}_i) = U(J) + \bar{\Psi}(\boldsymbol{g}, \boldsymbol{h}_i), \tag{17}$$

where U and $\bar{\Psi}$ represent the volumetric and isochoric response of the material, respectively. A canonical relation between the Lagrangian stresses, moduli, and the free-energy function can be established as

$$\boldsymbol{S} = 2\partial_{\boldsymbol{C}}\Psi(\boldsymbol{C}, \boldsymbol{H}_i) \qquad \text{and} \quad \mathbb{C} = 2\partial_{\boldsymbol{C}}\boldsymbol{S} = 4\partial^2_{\boldsymbol{C}\boldsymbol{C}}\Psi(\boldsymbol{C}, \boldsymbol{H}_i), \tag{18}$$

where $\boldsymbol{S}$ is the second Piola–Kirchhoff tensor and $\mathbb{C}$ is the Lagrangian moduli. The volumetric and isochoric parts of the second Piola–Kirchhoff stress read

$$\boldsymbol{S} = \boldsymbol{S}^{\text{vol}} + \boldsymbol{S}^{\text{iso}} \quad \text{with} \quad \boldsymbol{S}^{\text{vol}} := 2\partial_{\boldsymbol{C}}U(J) \quad \text{and} \quad \boldsymbol{S}^{\text{iso}} := 2\partial_{\boldsymbol{C}}\bar{\Psi}(\bar{\boldsymbol{C}}, \boldsymbol{H}_i). \tag{19}$$

Similarly, a canonical relation between the Helmholtz free-energy function, the Kirchhoff stresses, and the Eulerian moduli can be established as

$$\boldsymbol{\tau} = 2\partial_{\boldsymbol{g}}\Psi(\boldsymbol{g}; \boldsymbol{h}_i) \qquad \text{and} \quad \mathbb{C} = 2\partial_{\boldsymbol{g}}\boldsymbol{\tau} = 4\partial^2_{\boldsymbol{g}\boldsymbol{g}}\Psi(\boldsymbol{g}; \boldsymbol{F}, \boldsymbol{h}_i). \tag{20}$$

The Kirchhoff stresses can as well be decomposed as

$$\boldsymbol{\tau} = \boldsymbol{\tau}^{\text{vol}} + \boldsymbol{\tau}^{\text{iso}} \quad \text{with} \quad \boldsymbol{\tau}^{\text{vol}} := 2\partial_{\boldsymbol{g}}U(J) \quad \text{and} \quad \boldsymbol{\tau}^{\text{iso}} := 2\partial_{\boldsymbol{g}}\bar{\Psi}(\boldsymbol{g}, \boldsymbol{h}_i). \tag{21}$$

Herein, the volumetric part of the Lagrangian/Eulerian stresses read

$$\boxed{\boldsymbol{S}^{\text{vol}} = p\boldsymbol{C}^{-1} \quad \text{and} \quad \boldsymbol{\tau}^{\text{vol}} = p\boldsymbol{g}^{-1} \quad \text{where} \quad p = JU'(J)} \tag{22}$$

represents the hydrostatic negative pressure. The isochoric part of the second Piola Kirchhoff stress can be obtained by applying the chain rule

$$\boldsymbol{S}^{\text{iso}} = 2\left[\frac{\partial\bar{\Psi}}{\partial\bar{I}_1}\frac{\partial\bar{I}_1}{\partial\bar{\boldsymbol{C}}} + \sum_i^{n_f}\frac{\partial\bar{\Psi}}{\partial E_i}\frac{\partial E_i}{\partial\bar{\boldsymbol{C}}}\right] : \frac{\partial\bar{\boldsymbol{C}}}{\partial\boldsymbol{C}}\,. \tag{23}$$

Substituting the Eqs. (8) and (12) into Eq. (23) and by rearranging the terms, finally gives the generalized structure tensor-based representation of stresses for an anisotropic hyperelastic solid

$$\boldsymbol{S}^{\text{iso}} = \bar{\boldsymbol{S}} : \mathbb{Q} \qquad\qquad \boldsymbol{\tau}^{\text{iso}} = \bar{\boldsymbol{\tau}} : \mathbb{P}$$

$$\boxed{\boldsymbol{S}^{\text{iso}} = \left[2\psi_1\boldsymbol{G}^{-1} + 2\sum_i^{n_f}\psi_i\boldsymbol{H}_i\right] : \mathbb{Q}} \quad \overset{\text{push-forward}}{\rightsquigarrow} \quad \boxed{\boldsymbol{\tau}^{\text{iso}} = \left[2\psi_1\bar{\boldsymbol{b}} + 2\sum_i^{n_f}\psi_i\boldsymbol{h}_i\right] : \mathbb{P}} \tag{24}$$

with

$$\psi_1 = \partial_{I_1}\bar{\Psi} \quad \text{and} \quad \psi_i = \partial_{E_i}\bar{\Psi}. \tag{25}$$

In the above, the Lagrangian deviatoric projection tensor is defined as

$$\mathbb{Q} = \partial_{\boldsymbol{C}} \bar{\boldsymbol{C}} = J^{-2/3}\left(\mathbb{I} - \tfrac{1}{3}\boldsymbol{C} \otimes \boldsymbol{C}^{-1}\right) \quad \text{where} \quad \mathbb{I}_{AB}{}^{CD} = \frac{1}{2}(\delta_A{}^C\delta_B{}^D + \delta_A{}^D\delta_B{}^C) \tag{26}$$

is the fourth order symmetric identity tensor. Moreover, we define the Eulerian fourth-order symmetric identity and deviatoric projection tensors as follows

$$\mathbb{I}_{g^{-1}}{}^{abcd} = \frac{1}{2}(\delta^{ac}\delta^{bd} + \delta^{ad}\delta^{bc}) \quad \text{and} \quad \mathbb{P}_{ab}{}^{cd} = \frac{1}{2}(\delta_a{}^c\delta_b{}^d + \delta_a{}^d\delta_b{}^c) - \frac{1}{3}(\delta_{ab}\delta^{cd}). \tag{27}$$

In the proposed data-driven constitutive framework, the derivative expressions ψ_1 and ψ_i in Eq. (25) are estimated by B-spline interpolations where the control points that *a priori* satisfy the normalization and polyconvexity constraints, are trained via experimental data such as uniaxial tension, biaxial tension and shear experiments. The assembly procedure of a nth degree B-splines via *Cox-de Boor* recursion formula are briefly explained in Section 3.

2.5. Lagrangian/Eulerian moduli expressions

In line with (17), (19), and (21) the Lagrangian and Eulerian moduli expression can be decomposed into volumetric and isochoric parts

$$\mathbb{C} = \mathbb{C}^{\text{vol}} + \mathbb{C}^{\text{iso}} \qquad\qquad \mathfrak{C} = \mathfrak{C}^{\text{vol}} + \mathfrak{C}^{\text{iso}}. \tag{28}$$

The volumetric part of the moduli takes the following form

$$\boxed{\begin{aligned} \mathbb{C}^{\text{vol}} &= 2\partial_{\boldsymbol{C}}\boldsymbol{S}^{\text{vol}} = [(s+p)\boldsymbol{C}^{-1} \otimes \boldsymbol{C}^{-1} - 2p\mathbb{I}_{\boldsymbol{C}^{-1}}] \\ \mathfrak{C}^{\text{vol}} &= 2\partial_{\boldsymbol{g}}\boldsymbol{\tau}^{\text{vol}} = [(s+p)\boldsymbol{g}^{-1} \otimes \boldsymbol{g}^{-1} - 2p\mathbb{I}_{\boldsymbol{g}^{-1}}] \end{aligned}} \tag{29}$$

where $s = J^2U''(J)$. The isochoric part of the Lagrangian moduli expression can be written as

$$\boxed{\mathbb{C}^{\text{iso}} = 2\partial_{\boldsymbol{C}}\boldsymbol{S}^{\text{iso}} = \mathbb{Q}^T : \bar{\mathbb{C}} : \mathbb{Q} + 2\bar{\boldsymbol{S}} : \mathbb{M}} \tag{30}$$

with

$$\bar{\mathbb{C}} = 2\partial_{\bar{\boldsymbol{C}}}\bar{\boldsymbol{S}} \quad \text{and} \quad \mathbb{M} = \partial_{\boldsymbol{C}}\mathbb{Q}. \tag{31}$$

After some manipulations, the isochoric moduli can be reformulated as

$$\boxed{\mathbb{C}^{\text{iso}} = \mathbb{Q}^T : \bar{\mathbb{C}} : \mathbb{Q} + \frac{2}{3}\operatorname{tr}(\bar{\boldsymbol{S}})\mathbb{P}_{\boldsymbol{C}^{-1}} - \frac{2}{3}(\boldsymbol{C}^{-1} \otimes \boldsymbol{S}^{\text{iso}} + \boldsymbol{S}^{\text{iso}} \otimes \boldsymbol{C}^{-1})} \tag{32}$$

with

$$\mathbb{P}_{\boldsymbol{C}^{-1}} = J^{-2/3}\left(\mathbb{I}_{\boldsymbol{C}^{-1}} - \frac{1}{3}\boldsymbol{C} \otimes \boldsymbol{C}^{-1}\right) \quad \text{where} \quad \mathbb{I}_{\boldsymbol{C}^{-1}ABCD} = \frac{1}{2}(C^{-1}_{AC}C^{-1}_{BD} + C^{-1}_{AD}C^{-1}_{BC}). \tag{33}$$

A similar treatment leads to the Eulerian elasticity moduli

$$\boxed{\mathfrak{C}^{\text{iso}} = \mathbb{P}^T : (\bar{\mathfrak{C}} + \frac{2}{3}\operatorname{tr}(\bar{\boldsymbol{\tau}})\mathbb{I}_{\boldsymbol{g}^{-1}}) : \mathbb{P} - \frac{2}{3}(\boldsymbol{g}^{-1} \otimes \boldsymbol{\tau}^{\text{iso}} + \boldsymbol{\tau}^{\text{iso}} \otimes \boldsymbol{g}^{-1})} \tag{34}$$

for the isochoric response of the soft biological tissue. Insertion of the definition (31) into (34) leads to the Eulerian and Lagrangian moduli expressions

$$\boxed{\bar{\mathbb{C}} = 4\psi_1'\boldsymbol{G}^{-1} \otimes \boldsymbol{G}^{-1} + 4\sum_i^{n_f}\psi_i'\boldsymbol{H}_i \otimes \boldsymbol{H}_i} \overset{\text{push-forward}}{\rightsquigarrow} \boxed{\bar{\mathfrak{C}} = 4\psi_1'\bar{\boldsymbol{b}} \otimes \bar{\boldsymbol{b}} + 4\sum_i^{n_f}\psi_i'\boldsymbol{h}_i \otimes \boldsymbol{h}_i}. \tag{35}$$

For more details on the Lagrangian and Eulerian representation of isotropic and anisotropic hyperelasticity, we refer to Göktepe (2007) and Holzapfel et al. (2015).

Remark: The stresses and moduli expressions are derived based on the premise that tissue response purely deviatoric where the unimodular part of the deformation gradient $\boldsymbol{F}$ governs the constitutive response. This is the generally accepted approach in the computational mechanics of nearly incompressible materials such as rubber and soft biological tissues. However, the stresses $\{\bar{\boldsymbol{S}}, \bar{\boldsymbol{\tau}}\}$ and the respective moduli terms $\{\bar{\mathbb{C}}, \bar{\mathfrak{C}}\}$ can be replaced with $\{\boldsymbol{S}^{\text{iso}}, \boldsymbol{\tau}^{\text{iso}}\}$ and $\{\mathbb{C}^{\text{iso}}, \mathfrak{C}^{\text{iso}}\}$ provided that appropriate normalization conditions for the stresses are implemented.

3. Data-driven anisotropic hyperelasticity

3.1. Free-energy function

3.1.1. Principle of material objectivity

Let $\boldsymbol{x}^+ = \boldsymbol{Q}(t)\boldsymbol{x} + \boldsymbol{c}(t)$ denote the superimposed rigid body motion along with $\boldsymbol{Q}(t) \in \mathcal{SO}(3)$ belonging to the special orthogonal group. The principle of *material objectivity* (PMO) or the principle of *material frame indifference* states that

$$\hat{\psi}(\boldsymbol{F}^+, \boldsymbol{X}) = \hat{\psi}(\boldsymbol{F}, \boldsymbol{X}). \quad \text{for} \quad \boldsymbol{F}^+ = \boldsymbol{Q}\boldsymbol{F} \tag{36}$$

Recall that, in this regard, unlike the Finger tensor $\boldsymbol{b}^{+} = \boldsymbol{Q}\boldsymbol{b}\boldsymbol{Q}^T$, the right Cauchy–Green tensor $\boldsymbol{C}^{+} = \boldsymbol{C}$ satisfies the PMO. The PMO is *a priori* satisfied if $\psi = \hat{\psi}(\boldsymbol{C})$. The anisotropic invariants $E_i = \boldsymbol{H}_i : \bar{\boldsymbol{C}}$ satisfy the material frame indifference *a priori*.

3.1.2. Principle of material symmetry

Anisotropic materials possess certain symmetry properties due to their microstructure. The material symmetry is characterized in terms of the symmetry group $\mathcal{G} \subset \mathcal{SO}(3)$ which is the set of rotations that leaves the microstructure of the material unchanged with regard to rotations superimposed to the reference configuration. The material symmetry is formulated by an invariance principle dual to the principle of material objectivity: The constitutive equations should be invariant with respect to rotations superimposed onto the reference configuration $\boldsymbol{X}^{\star} = \boldsymbol{Q}\boldsymbol{X}$ that belong to the symmetry group i.e.,

$$\psi(\boldsymbol{F}^{\star}, \boldsymbol{X}) = \psi(\boldsymbol{F}, \boldsymbol{X}) \quad \forall\, \boldsymbol{Q} \in \mathcal{G} \subset \mathcal{SO}(3) \tag{37}$$

in terms of $\boldsymbol{F}^{\star} = \boldsymbol{F}\boldsymbol{Q}^T$ and the proper orthogonal rotation tensor $\boldsymbol{Q} \in \mathcal{G} \subset \mathcal{SO}(3)$. For an isotropic material the symmetry group $\mathcal{G}$ coincides with the entire $\mathcal{SO}(3)$, i.e. $\mathcal{G} = \mathcal{SO}(3)$. The condition (37) is a further restriction for the free-energy function ψ. Recall that $\boldsymbol{C}^{\star} = \boldsymbol{Q}\boldsymbol{C}\boldsymbol{Q}^T$. Principle of material objectivity together with the notion of *material symmetry* postulate specific form of a free-energy functions in the sense

$$\psi(\boldsymbol{F}) = \tilde{\psi}(\lambda_1, \lambda_2, \lambda_3) \qquad \text{or} \qquad \psi(\boldsymbol{F}) = \hat{\psi}(I_1, I_2, I_3), \tag{38}$$

where the free-energy can be described either in terms of principal invariants or principal stretches that are invariant with respect to superimposed rigid body rotations imposed on the reference or current configuration.

Transverse isotropy: The scalar-valued isotropic function of two tensor variables of the form $\psi = \psi(\boldsymbol{C}, \boldsymbol{H})$ must satisfy the condition

$$\psi(\bar{\boldsymbol{C}}^{\star}, \boldsymbol{H}^{\star}) = \psi(\bar{\boldsymbol{C}}, \boldsymbol{H}) \tag{39}$$

for $\boldsymbol{H}^{\star} = \boldsymbol{Q}\boldsymbol{H}\boldsymbol{Q}^T$ for $\boldsymbol{Q}(t) \in \mathcal{SO}(3)$, see Holzapfel (2000). The identity (39) is a priori satisfied due to the invariance of $E_i = \bar{\boldsymbol{C}} : \boldsymbol{H} = \bar{\boldsymbol{C}}^{\star} : \boldsymbol{H}^{\star}$ for transverse isotropic solids described in terms of a generalized structure tensor $\boldsymbol{H}$.

3.1.3. Principle of irreversibility

The *dissipation inequality*, or the *Clausius-Duhem inequality* reads $\mathcal{D}_{loc} = \boldsymbol{P} : \dot{\boldsymbol{F}} - \dot{\psi} \geq 0$. For an elastic, reversible process, and for $\psi = \psi(\boldsymbol{F})$, the dissipation inequality reduces to

$$\mathcal{D}_{loc} = \boldsymbol{P} : \dot{\boldsymbol{F}} - \partial_{\boldsymbol{F}}\psi(\boldsymbol{F}) : \dot{\boldsymbol{F}} = 0 \quad \rightsquigarrow \quad \boldsymbol{P} = \partial_{\boldsymbol{F}}\psi(\boldsymbol{F}). \tag{40}$$

In line with Eq. (40), similar derivations can be made for

$$\boldsymbol{S} = 2\partial_{\boldsymbol{C}}\psi(\boldsymbol{C}) \quad \text{and} \quad \boldsymbol{\tau} = 2\partial_{\boldsymbol{g}}\psi(\boldsymbol{g}; \boldsymbol{F}). \tag{41}$$

Herein, the first Piola–Kirchhoff $\boldsymbol{P}$, the second Piola–Kirchhoff $\boldsymbol{S}$ and Kirchhoff $\boldsymbol{\tau}$ stress tensors are related to one another through appropriate pull-back and push-forward relations

$$\boldsymbol{P} = \boldsymbol{F}\boldsymbol{S} \quad \text{and} \quad \boldsymbol{\tau} = \boldsymbol{F}\boldsymbol{S}\boldsymbol{F}^T. \tag{42}$$

The existence of a relation between the stress tensor and the potential ψ in the sense of Eq. (40), (41) is the basic postulate of hyperelasticity.

3.1.4. Normalization and growth conditions

The free-energy function is subjected to the following physical normalization conditions

$$\psi(\boldsymbol{1}) = 0 \qquad \text{and} \qquad \partial_{\boldsymbol{F}}\psi(\boldsymbol{1}) = \boldsymbol{0}. \tag{43}$$

The first proposition corresponds to the minimum free-energy at undeformed ground-state. The second proposition results from the *stationarity condition* of the free-energy at ground state,

$$\partial_{\boldsymbol{F}}\psi_{\boldsymbol{F}=\boldsymbol{1}} : \delta\boldsymbol{F} = 0 \qquad \rightsquigarrow \qquad \partial_{\boldsymbol{F}}\psi(\boldsymbol{1}) = \boldsymbol{0} \tag{44}$$

and refers to the stress-free reference configuration. The growth conditions

$$\psi \to \infty \quad \text{for} \quad J \to 0^+ \qquad \text{and} \qquad \psi \to \infty \quad \text{for} \quad J \to \infty, \tag{45}$$

are natural requirements that ensure non-penetrable physical deformations and monotonicity of the free-energy function, respectively. The growth condition (45) is *a priori* eliminated since the (large) deviations of $\det \boldsymbol{F}$ from 1 are penalized. Similar natural conditions can as well be imposed for

$$\psi \to \infty \quad \text{for} \quad \boldsymbol{F} \to \infty \tag{46}$$

where $(\bullet) = [(\bullet) \cdot (\bullet)]^{1/2}$ is the norm operator. Eq. (46) can equivalently be replaced by

$$\psi \to \infty \quad \text{for} \quad I_1 \to \infty \qquad \text{where} \qquad \psi \to \infty \quad \text{for} \quad I_1 \to 0^+ \tag{47}$$

is *a priori* eliminated as $I_1 \to 0^+$ would imply $\lambda_i \to 0^+$, which violate the incompressibility assumption $\lambda_1 \lambda_2 \lambda_3 = 1$.

$$\psi \to \infty \quad \text{for} \quad E_i \to \infty \qquad \text{where} \qquad \psi \to \infty \quad \text{for} \quad E_i \to 0^+ \tag{48}$$

is *a priori* eliminated due to the tension-only condition. In our proposed model we determine numerically the derivative of the free energy function that governs the mechanical response of the tissue. To do so, the derivatives of the free energy function are approximated by B-spline interpolations as described in what follows.

3.2. Computational geometry: Concept of B-splines

B-splines are essentially Bézier curves that are added end-to-end. In this way, more control points are added to increase the fitting capabilities of the resulting B-spline without having to increase the polynomial order of the curve. B-spline $C(\xi)$ and its derivative can be written in summation form

$$C(\xi) = \sum_{k=1}^{n} \mathcal{N}_k^p(\xi)\mathcal{P}_k \qquad \text{and} \qquad C'(\xi) = \sum_{k=1}^{n} \mathcal{N}_k^{p\,\prime}(\xi)\mathcal{P}_k, \tag{49}$$

where $\mathcal{N}_k^p(\xi)$ and $\mathcal{N}_k^{p\,\prime}(\xi)$ are Bernstein basis functions and their derivatives; with p being the polynomial degree of the basis function and $\mathcal{P}_k$ are the control points, or vertices, associated with the basis functions. The number of control points is n which results in a B-spline that consists of $n-p$ number of Bézier curves or elements. $\mathcal{N}_k^p(\xi)$ and $\mathcal{N}_k^{p\,\prime}(\xi)$ in Eq. (49) are obtained from the Cox-de Boor recursion formula

$$\mathcal{N}_k^0(\xi) = \left| \begin{array}{ll} 0, & \text{if} \quad \xi_k \leq \xi < \xi_{k+1} \\ 1, & \text{otherwise} \end{array} \right. \tag{50}$$

along the given knot span. Basis functions $\mathcal{N}_k^p$ and their derivatives $\mathcal{N}_k^{p\,\prime}$ for $p > 0$ are computed through

$$\mathcal{N}_k^p(\xi) = \frac{\xi - \xi_k}{\xi_{k+p} - \xi_k}\mathcal{N}_k^{p-1}(\xi) + \frac{\xi_{k+p+1} - \xi}{\xi_{k+p+1} - \xi_{k+1}}\mathcal{N}_{k+1}^{p-1}(\xi), \tag{51}$$

$$\mathcal{N}_k^{p\,\prime}(\xi) = \frac{p}{\xi_{k+p} - \xi_k}\mathcal{N}_k^{p-1}(\xi) + \frac{p}{\xi_{k+p+1} - \xi_{k+1}}\mathcal{N}_{k+1}^{p-1}(\xi), \tag{52}$$

where $\xi_{\hat{k}}$ with $\hat{k} = \{1, 2, \dots, m\}$ are the so-called knots with a total number of m knots. Obvious from the Cox-de Boor formula in Eq. (50), support of every basis function $\mathcal{N}_k^p(t)$ is $p+1$ knot spans. Given the polynomial degree p and the number of control points n of the B-spline, the number of knots is found as $m = p+n+1$. By definition of the Cox-de Boor formula, B-splines are not defined in the first and last p intervals between knots. To circumvent this issue and have a defined spline between the first and the last knots we use the so-called open-knot vectors where the first and the last knots are repeated $p+1$ times in the knot vector. At the knots, basis functions of degree p have $p-r$ continuous derivatives where r is the number of times a knot is repeated. In this study, we do not repeat intermediate knots, whereas only the start and end nodes are repeated $p+1$ times as per open knot definition. Fig. 3 shows examples of different B-splines with various degrees and control points.

3.3. Data-driven constitutive functions

In the invariant-based data-driven formulation of hyperelasticity, the partial derivatives ψ_1 and ψ_i can be interpolated as

$$\psi_1 = \sum_{k=1}^{n} \mathcal{N}_k^p(I_1)\mathcal{P}_k^1 \quad \text{and} \quad \psi_i = \sum_{k=1}^{n} \mathcal{N}_k^p(E_i)\mathcal{P}_k^i. \quad \text{with} \quad i = \{f, s, fs\} \quad \text{or} \quad i = \{4, 6\} \tag{53}$$

where $\mathcal{N}_i^p$ are the basis functions of order p and $\mathcal{P}_k^1$, $\mathcal{P}_k^i$ are the control points replacing the material parameters in the constitutive equations.

3.4. Polyconvexity

The constitutive model of physical material is bound to satisfy certain mathematical constraints, which are material frame indifference, (quasi-)convexity, and growth conditions. Material frame indifference, or known as the objectivity condition, is satisfied a priori thanks to the use of the right Cauchy–Green tensor and its invariants in the constitutive model. In addition, growth conditions are satisfied by a proper choice of volumetric strain energy function $U(J)$. On the other hand, the convexity condition needs special treatment. The elasticity problem can be formulated as a minimization problem,

$$\inf_{\boldsymbol{\varphi} \in \mathcal{W}^{1,p}(\mathcal{B})} \left| I(\boldsymbol{\varphi}) = \int_{\mathcal{B}} \Psi(\nabla\boldsymbol{\varphi})\, dV \mid \boldsymbol{\varphi} = \bar{\boldsymbol{\varphi}} \text{ on} \partial\mathcal{B} \right\| \tag{54}$$

where the deformation map $\boldsymbol{\varphi}$ is the minimizer of the functional $I(\boldsymbol{\varphi})$ and belongs to the Sobolev space $\boldsymbol{\varphi} \in \mathcal{W}^{1,p}(\mathcal{B})$. There exists a solution to the minimization problem given in Eq. (54), if the free energy function Ψ is convex (Ciarlet, 1988). However, convexity condition is a too strong requirement and in some cases unphysical. The notion of polyconvexity was proposed by Ball (1976) which is a weaker convexity condition and does not violate any physical phenomena. Polyconvexity requires $\tilde{\Psi}(\boldsymbol{F}, \mathrm{cof}[\boldsymbol{F}], \det[\boldsymbol{F}])$ to be convex with respect to $\boldsymbol{F}$, $\mathrm{cof}[\boldsymbol{F}]$ and $\det[\boldsymbol{F}]$, respectively. In invariant-based formulation, polyconvexity of the free energy

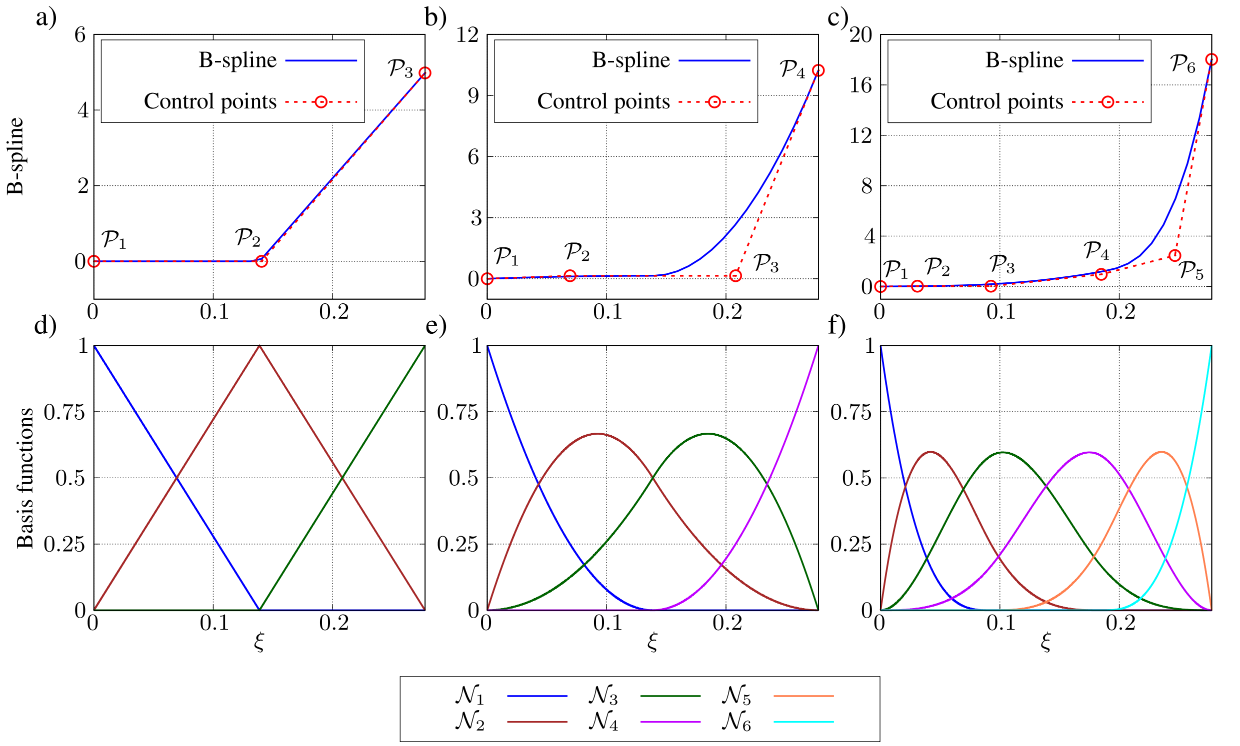

Fig. 3. (a) Linear, (b) quadratic, and (c) cubic B-spline interpolations with (d) linear, (e) quadratic, and (f) cubic basis functions.

function $\hat{\Psi}(I_1, J, E_i, \dots)$ is ensured given that it is convex with respect to the invariants $\{I_1, J, E_i, \dots\}$ as discussed in Schröder and Neff (2003). Gasser et al. (2006) has proven that for

$$\psi_i(E_i) > 0 \quad \text{and} \quad \psi_{ii}(E_i) > 0 \tag{55}$$

the anisotropic part of the free-energy function is polyconvex. For the growth and polyconvexity requirements for ψ_1, we refer to the part I (Dal et al., 2023a). Its implication on our model is that the B-splines representing the first derivatives of the free energy function, i.e. $\psi_1(I_1)$ and $\psi_i(E_i)$, need to be non-decreasing so that the free energy function is polyconvex. This is achieved by enforcing a simple relation

$$\mathcal{P}^a_{i+1} - \mathcal{P}^a_i \geq 0 \quad a = \{f, s, fs\} \quad \text{or} \quad a = \{4, 6\} \tag{56}$$

for the control points that ensure monotonic Bèzier curves. Similarly, they are convex function of E_i given that the control polygon is convex (Davis, 1975). B-splines can be represented as Bèzier curves joined end-to-end. Therefore B-splines inherit the convexity properties from the Bèzier curves. These properties of B-splines imply that, control points $\mathcal{P}^a_i$ belonging to each free-energy contribution need to be in increasing order, in order to ensure the polyconvexity of the free energy function. We impose this condition at the data-training phase as an inequality constraint, which is handled by Matlab's optimization function Fmincon.

4. Model predictions for soft biological tissues under homogeneous deformations

In this section, we validate the data-driven modeling approach that was outlined in Section 3. In doing so, we obtain optimized control point values by fitting them to experimental data, assuming the number of control points and B-spline degree are known. We show the capability of the model to predict varying hyperelastic mechanical behavior, observed in experimental characterizations of various types of biological soft tissues. In particular, we calibrate the model using triaxial shear data for myocardium tissue (Sommer et al., 2015), equibiaxial tension data for abdominal aneurysmic aorta (AAA) tissue (Niestrawska et al., 2016), uniaxial tension data for linea alba tissue (Cooney et al., 2016), and uniaxial tension data for rectus sheath tissue (Martins et al., 2012). We used various numbers of control points and basis function degrees in fitting the data The optimized control points and sensitivity analysis can be found in the Appendix. The quality of fit metric χ^2 for different loading conditions is computed using predicted stresses $P_{\alpha\beta}$, $\sigma_{\alpha\beta}$ and experimental counterparts $P^{\text{exp}}_{\alpha\beta}$, $\sigma^{\text{exp}}_{\alpha\beta}$ as follows

$$\chi^2 = \sum_{\alpha\beta\in \boldsymbol{m}_{\text{exp}}} \sum_{i=1}^{N^{\text{exp}}_{\alpha\beta}} \frac{\left(P_{\alpha\beta}(\lambda_i) - P^{\text{exp}}_{\alpha\beta}(\lambda_i)\right)^2}{P^{\text{exp}}_{\alpha\beta}(\lambda_i)} \tag{57}$$

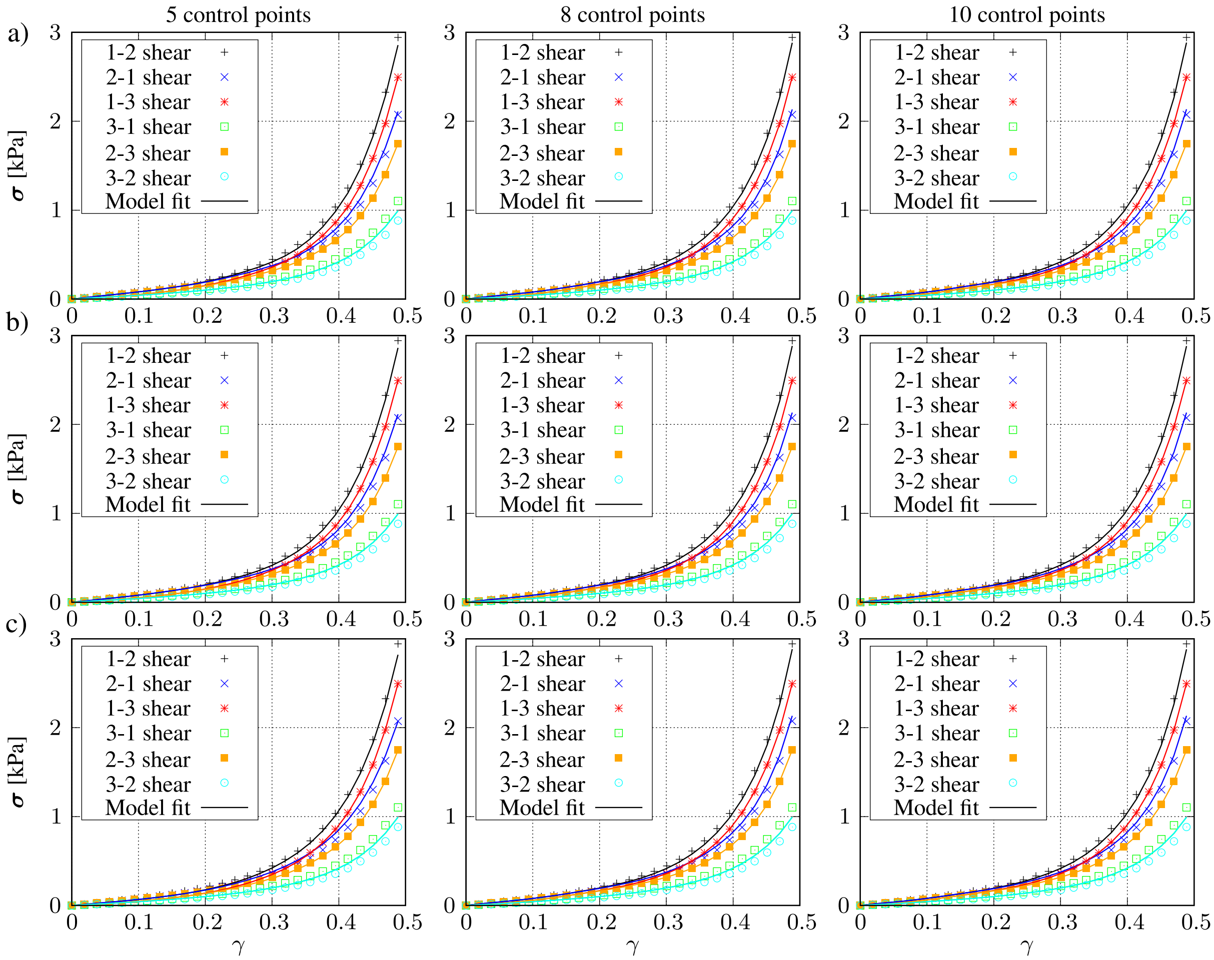

Fig. 4. Predictions for triaxial shear dataset for myocardium tissue (Niestrawska et al., 2016) with the 5 (column #1), 8 (column #2), 10 (column #3) of control points and with (a) quadratic, (b) cubic, (c) quartic basis functions.

where $\boldsymbol{m}_{\text{exp}}$ represents the set of deformation modes performed in the equibiaxial, uniaxial, and triaxial experiments ($\alpha\beta$), specifically $\boldsymbol{m}_{\text{et}} = \{(11), (22)\}$ and $\boldsymbol{m}_{\text{ut}} = \{(11), (22)\}$, while $\boldsymbol{m}_{\text{shear}}$ denotes the set of shear modes performed in these experiments, which includes $\{(12), (21), (13), (31), (23), (32)\}$. Additionally, $N_{\alpha\beta}^{\text{exp}}$ represents the number of data points collected in a given experiment. During the optimization phase, the structural features of the tissues remained constant while the control points were optimized. In fitting the material model, stresses are calculated at a single material point assuming homogeneous deformation states. The volumetric part of the free energy function $U(J)$ in (17) was excluded and the pressure term was obtained from boundary conditions enforcing exactly the incompressible deformation state under uniaxial and biaxial deformations.

4.1. Predictions of the data-driven model for myocardium dataset

In the first example, we fit the data-driven model to the triaxial shear dataset for myocardium (Sommer et al., 2015). Myocardial tissue shows highly nonlinear orthotropic material behavior which can be characterized by three orthonormal basis vectors: fiber $\boldsymbol{f}$, sheet $\boldsymbol{s}$, and normal $\boldsymbol{n}$ (Dokos et al., 2002; Sommer et al., 2015), which coincide with $\boldsymbol{e}_1, \boldsymbol{e}_2$ and $\boldsymbol{e}_3$ directions. Sommer et al. (2015) investigated the mechanical behavior and the microstructure of the myocardium. They observed that myocardial tissue has dispersed fiber structure in both fiber and sheet directions. Accordingly, we use the Planar von Mises fiber dispersion model that we explained in Section 2.3 together with the dispersion parameters $\kappa_f = 0.08$ and $\kappa_s = 0.09$ identified in Sommer et al. (2015). In Fig. 6, the polar plots of the density distribution function that correspond to the dispersion of fibers in myocardium tissue are given. In fitting the triaxial shear data, we employ four invariants of deformation, I_1, E_f, E_s, E_{fs}; therefore four B-splines $\psi_1(I_1)$, $\psi_f(E_f)$, $\psi_s(E_s)$, $\psi_{fs}(E_{fs})$ in representing the derivatives of the strain energy function. The deformation gradient $\boldsymbol{F}_{\alpha\beta}$ for the shear mode $\alpha\beta$ is

$$\boldsymbol{F}_{\alpha\beta} = \boldsymbol{1} + \gamma \boldsymbol{e}_\beta \otimes \boldsymbol{e}_\alpha \quad \text{with} \quad \alpha, \beta = \{1, 2, 3\},\ \alpha \neq \beta\ , \tag{58}$$

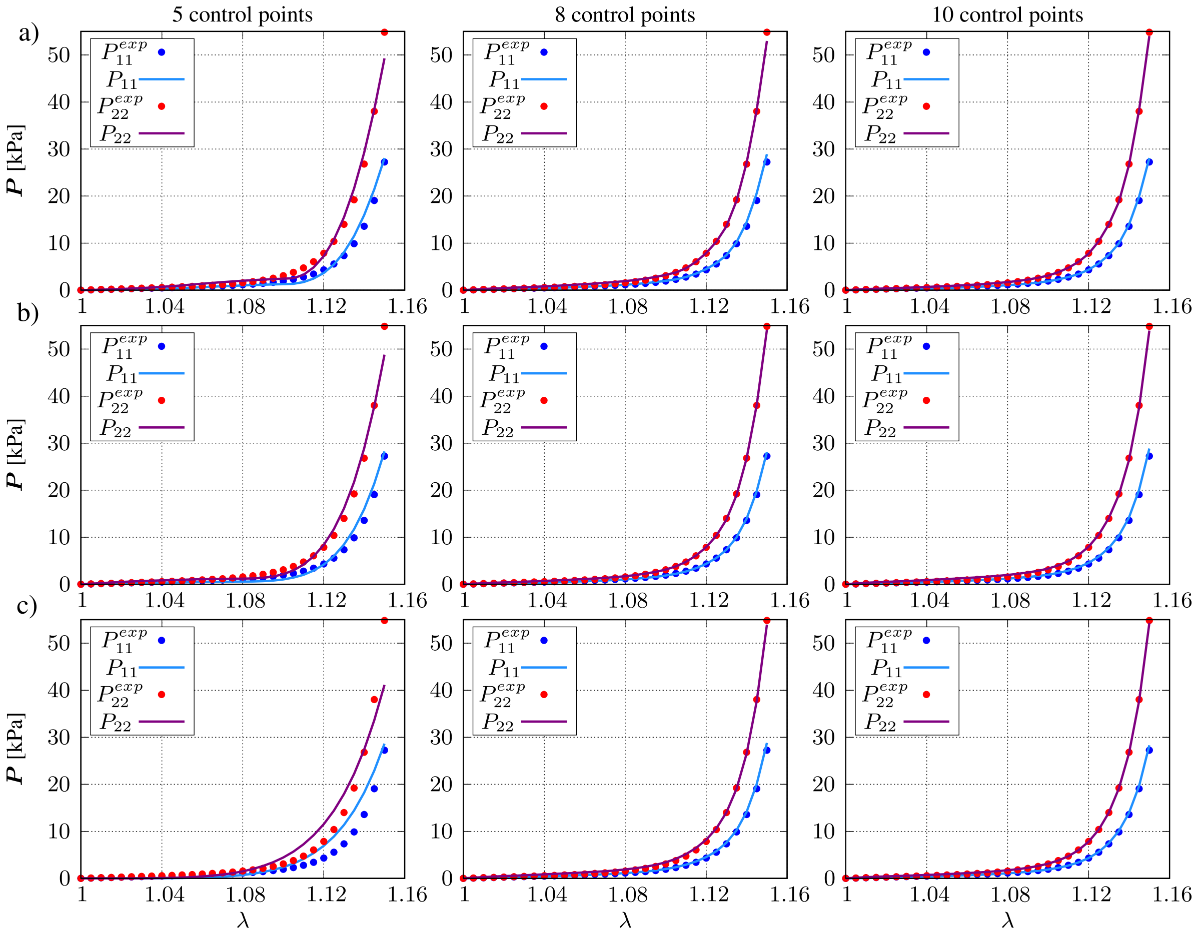

Fig. 5. Predictions for ET dataset for AAA tissue (Niestrawska et al., 2016) with the 5 (column #1), 8 (column #2), 10 (column #3) of control points and with (a) quadratic, (b) cubic, (c) quartic basis functions.

where γ is the amount of shear. Fitting results of 6 different shear modes with different numbers of control points and degrees can be seen in Fig. 4. Optimized control point values for four B-spline functions can be found in the Appendix. The best prediction has been obtained via PO4/CP10.[2]

4.2. Predictions of the data-driven model for abdominal aneurysmic aorta (AAA) dataset

In the second example, we fit the data-driven model to equibiaxial tension dataset for AAA tissue (Niestrawska et al., 2016). AAA tissue has two families of fibers symmetric around the circumferential direction of the aorta. Schriefl et al. (2012a,b, 2013, 2012c) showed that aorta has both in-plane and out-of-plane dispersion of fibers. Following this observation, Holzapfel et al. (2015) proposed using a bivariate von Mises density distribution function to model the dispersed fiber orientation of the tissue. In this particular instance, we followed experimental observations and utilized two types of fiber families that follow a bivariate von Mises density function. The angle between the average fiber directions and the circumferential direction is $\alpha = 26°$, while the dispersion parameters are $\kappa_{ip} = 0.29$ and $\kappa_{op} = 0.397$ (Niestrawska et al., 2016). The polar plots of the density distribution function that correspond to the in-plane and out-of-plane dispersion of fibers are given in Fig. 6a. In fitting the equibiaxial stretch data, we employ three invariants of deformation, $I_1,\ E_4,\ E_6$; therefore three B-splines $\psi_1(I_1),\ \psi_4(E_4)$, and $\psi_6(E_6)$ in representing the derivatives of the strain energy function. The deformation gradient $\boldsymbol{F}$ for equibiaxial stretching assuming incompressibility is

$$\boldsymbol{F} = \lambda\,(\boldsymbol{e}_1 \otimes \boldsymbol{e}_1 + \boldsymbol{e}_2 \otimes \boldsymbol{e}_2) + \frac{1}{\lambda^2}\,\boldsymbol{e}_3 \otimes \boldsymbol{e}_3\ , \tag{59}$$

[2] POX/CPY : B-spline curve of polynomial order X consisting of Y control (vertex) points.

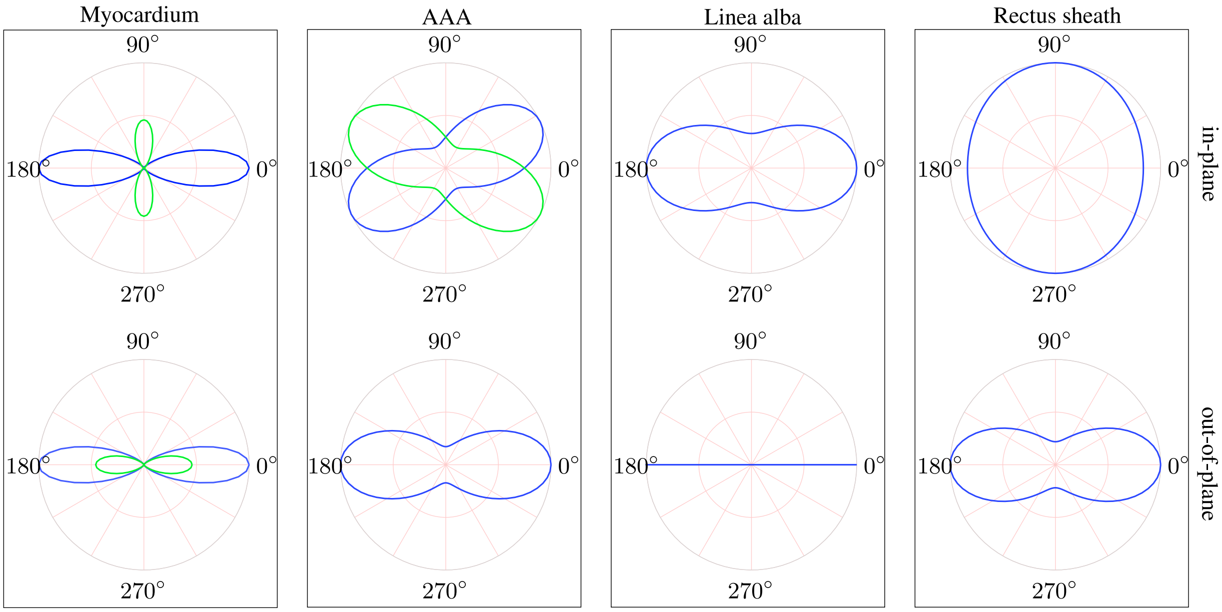

Fig. 6. The polar plots of in-plane and out-of-plane density distributions for myocardium, abdominal aortic aneurysm (AAA), linea alba and rectus sheath.

where λ is the amount of stretch. Fitting results of equibiaxial tension dataset with different numbers of control points and degrees can be seen in Fig. 5 and in Appendix. The best fit to experimental data is achieved by PO2/CP10. Moreover, utilizing 6 control points results in a reasonably accurate prediction for the three distinct basis functions.

4.3. Predictions of the data-driven model for linea alba dataset

As the third example, we applied the data-driven model to the uniaxial tension dataset for linea alba (Cooney et al., 2016). Linea alba is an anisotropic tissue with a single family of fibers. Cooney et al. (2016) did not report any observation about fiber dispersion, therefore previously fitted parameters (Dal et al., 2023a) of $\kappa_{ip} = 0.645$ and $\kappa_{op} = 0.499$ were used, along with a mean fiber direction that coincided with the direction of $\boldsymbol{e}_2 = \boldsymbol{M}_4$. The polar plots of the density distribution function that corresponds to the dispersion of fibers embedded in linea alba tissue are given in Fig. 6. Cooney et al. (2016) conducted uniaxial tension experiments with samples cut in both longitudinal and transverse directions, referring to their respective anatomical axes. In fitting the uniaxial stretch data, we employ two invariants of deformation, I_1, E_4; therefore two B-splines $\psi_1(I_1)$, $\psi_4(E_4)$ in representing the derivatives of the strain energy function. The deformation gradient $\boldsymbol{F}_{\alpha\alpha}$ for the stretch mode $\alpha\alpha$ assuming incompressibility is

$$\boldsymbol{F}_{\alpha\alpha} = \lambda(\boldsymbol{e}_\alpha \otimes \boldsymbol{e}_\alpha) + \frac{1}{\sqrt{\lambda}}(\boldsymbol{e}_\beta \otimes \boldsymbol{e}_\beta + \boldsymbol{e}_3 \otimes \boldsymbol{e}_3) \quad \text{with} \quad \alpha, \beta = \{1, 2\},\ \alpha \neq \beta\ , \tag{60}$$

where λ is the amount of stretch. Fitting results of the uniaxial tension dataset with varying numbers of control points and degrees can be seen in Fig. 7 and in Appendix. PO4/CP10 provided the best predictions over the linea alba dataset. It has been observed that when using quadratic, cubic, and quartic basis functions, the quality of fit remains almost unaffected by the number of control points used beyond 8.

4.4. Predictions of the data-driven model for rectus sheath dataset

In the last example, we used the rectus sheath testing dataset from Martins et al. (2012) to calibrate the data-driven model. Rectus sheath tissue involves a single family of fiber similar to linea alba tissue. The authors have not reported histology information of the tissue, therefore previously fitted parameters (Dal et al., 2023a) of $\kappa_{ip} = 0.522$ and $\kappa_{op} = 0.390$ were used, along with a mean fiber direction that coincided with the direction of $\boldsymbol{e}_1 = \boldsymbol{M}_4$. Martins et al. (2012) conducted uniaxial stretching tests in longitudinal direction (fiber direction $\boldsymbol{e}_1 = \boldsymbol{M}_4$) and in transverse-fiber direction $\boldsymbol{e}_2$. The polar plots of the density distribution function that corresponds to the dispersion of fibers embedded in the rectus sheath are given in Fig. 6. The main goal of these test was to observe damage and rupture of the tissue samples. However, as we are interested in hyperelastic behavior, we constricted our focus on the region where no stress softening was observed. In fitting the uniaxial stretch data, we employ two invariants of deformation, I_1, E_4;

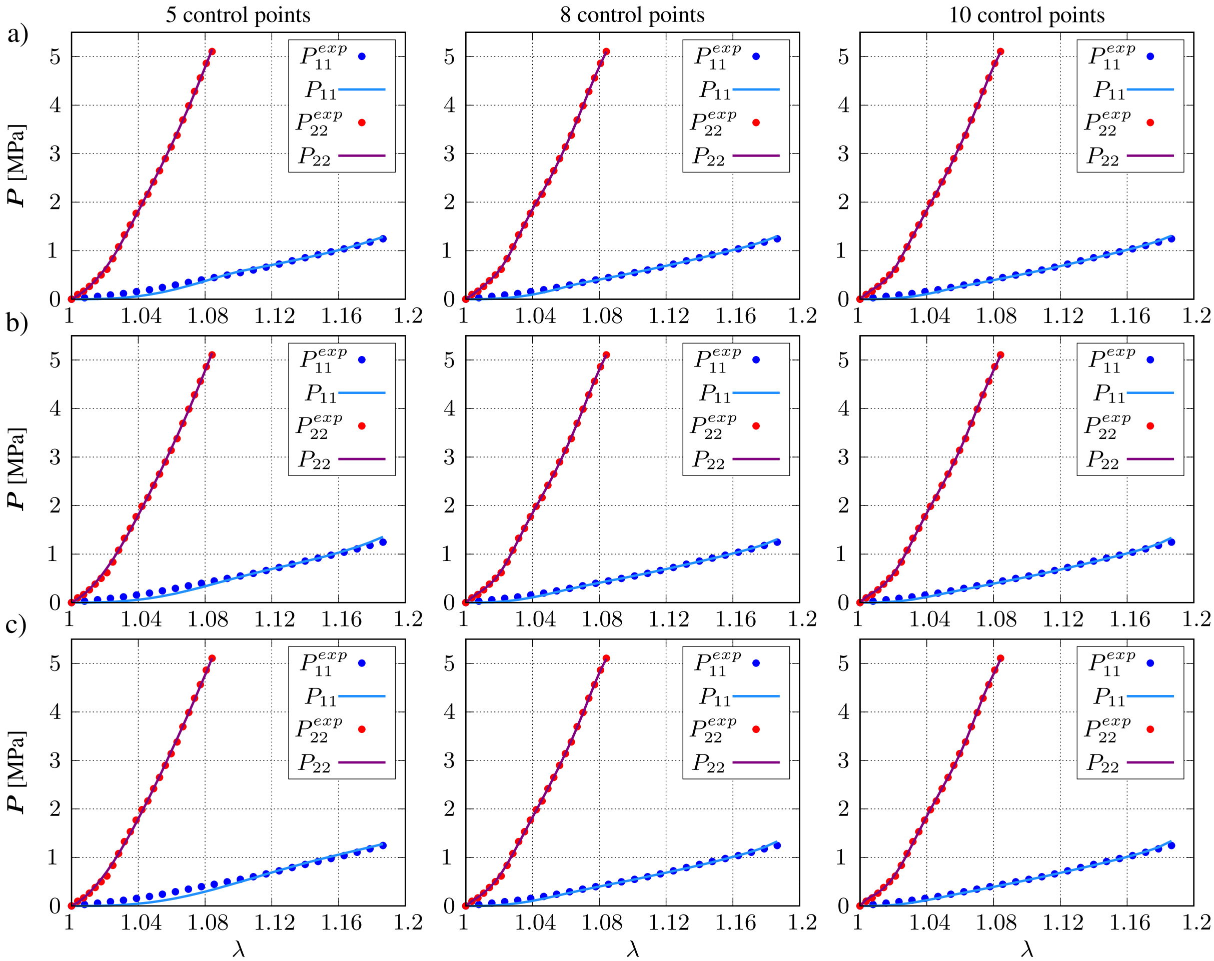

Fig. 7. Predictions for UT dataset for linea alba tissue (Cooney et al., 2016) with the 5 (column #1), 8 (column #2), 10 (column #3) of control points and with (a) quadratic, (b) cubic, (c) quartic basis functions.

therefore two B-splines $\psi_1(I_1)$, $\psi_4(E_4)$ in representing the derivatives of the strain energy function. Assuming incompressibility, the deformation gradient $\boldsymbol{F}_{\alpha\alpha}$ for the stretch mode $\alpha\alpha$ is

$$\boldsymbol{F}_{\alpha\alpha} = \lambda(\boldsymbol{e}_\alpha \otimes \boldsymbol{e}_\alpha) + \frac{1}{\sqrt{\lambda}}(\boldsymbol{e}_\beta \otimes \boldsymbol{e}_\beta + \boldsymbol{e}_3 \otimes \boldsymbol{e}_3) \quad \text{with} \quad \alpha, \beta = \{1, 2\},\ \alpha \neq \beta \tag{61}$$

where λ is the amount of stretch. Results of the model fitment to the stretch testing dataset can be seen in Fig. 8 and in Appendix, for varying numbers of control points and polynomial degrees. Surprisingly, PO2/CP5 yielded the most accurate prediction, contrary to our expectations. While increasing the number of control points improved the fit for other tissue datasets, this anomaly may be attributed to the optimization algorithm employed in this study. Employing a different optimization algorithm could alter the identified control points and improve the quality of fit.

4.5. *Investigation on synthetic dataset*

To assess the potential of the suggested model to discover existing models, we utilized a dataset manufactured using a previously proposed constitutive law. We hypothesized a soft tissue featuring two families of fibers under equibiaxial loading. The synthetic data was generated according to the Holzapfel et al. (2015) framework, as outlined below.

$$\Psi(\boldsymbol{C}, \boldsymbol{H}_i) = \frac{1}{2}\mu\left(I_1 - 3\right) + \frac{k_1}{2k_2}[\exp(k_2 E_i^2) - 1], \quad i = 1, 2. \tag{62}$$

In Fig. 9a, we demonstrated the proposed model's efficacy in uncovering the underlying constitutive law. We also examined the convergence of the quality of fit with the augmentation of data points. As depicted in Fig. 9c, approximately 50 data points suffice

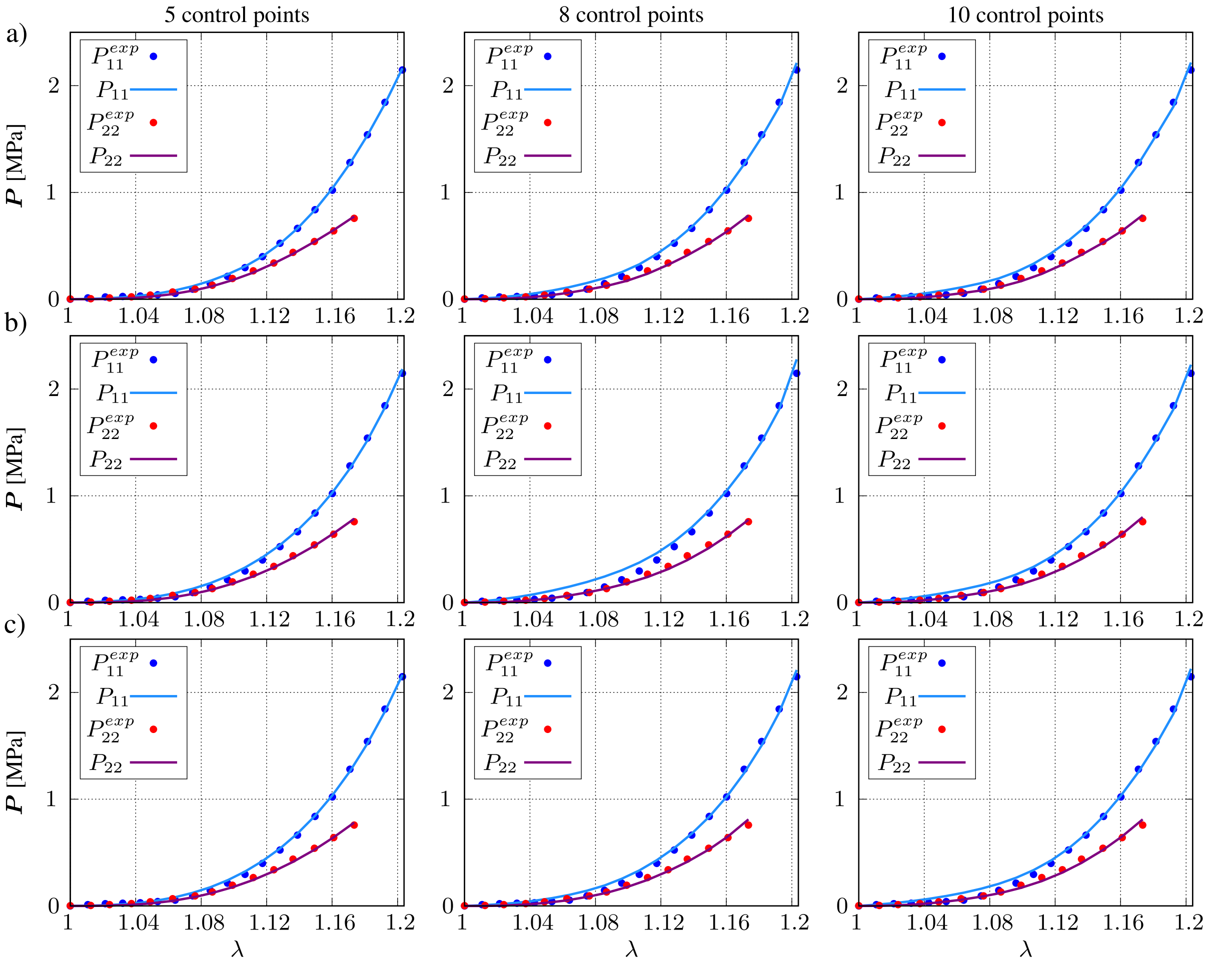

Fig. 8. Predictions for UT dataset for rectus sheath tissue (Martins et al., 2012) with the 5 (column #1), 8 (column #2), 10 (column #3) of control points and with (a) quadratic, (b) cubic, (c) quartic basis functions.

to discover the latent constitutive law. It is important to note that experimental measurements typically entail a degree of inherent noise. Hence, we extended our investigation to evaluate the model's ability to fit such noisy data. To simulate this scenario, we intentionally introduced Gaussian noise with a mean of zero and a standard deviation of 5% to the synthetic data obtained from the analytical model. Fig. 9b illustrates the data-driven model's robust capability to fit noisy data. B-spline is recognized as a valuable tool for interpolating data. However, they are prone to error when extrapolating data. To illustrate the extrapolation behavior of our current framework, we partitioned the synthetic dataset into training and validation sets. We calibrated the data-driven model using the training portion of the data and subsequently extrapolated the model to evaluate agreement with the validation data. B-Splines were extrapolated linearly into the validation data range. Stress–strain response resulting from this extrapolation behavior, is shown in Fig. 9d.

5. Representative numerical examples

In this section, we present the algorithmic treatment of our proposed material model, and we showcase the performance of finite element implementation. We implemented our constitutive model into the finite element software FEAP (Taylor, 2014), yet implementing it into any finite element software would be straightforward. FEAP utilizes `UMATIn` and `UMATLn` subroutines for user material implementations. In line with a deformation-driven solution procedure, the input of the user material subroutine is the deformation gradient $\boldsymbol{F}$ and the corresponding outputs are the Cauchy stress $\boldsymbol{\sigma}$ and Eulerian tangent moduli $\mathbb{c}$. The algorithm of the material subroutine is summarized in Algorithm 1, which represents a standard anisotropic hyperelastic material calculation. At step 4 of Algorithm 1, to evaluate ψ_i and ψ_i', we use B-spline functions given the material parameters: control points range of parametrization and the polynomial degree. Our B-spline implementation in FORTRAN language is about 110 lines long, replacing the analytical calculations of ψ_1, ψ_i and ψ_1', ψ_i' in conventional models. In our implementation we prioritized flexibility of the implementation over computational efficiency, however, it is possible to decrease the computational cost by circumventing the

Algorithm 1 Computation of stress and tangent expressions at the integration point level.

Input : $\boldsymbol{F}$
Output : $\boldsymbol{\tau}, \mathbb{c}$

Computation of deformation measures

`Calculate:` $\boldsymbol{F} \rightarrow I_1, J$	Eq. (7)
`Calculate:` $\boldsymbol{H}_i$	Eqs. ((10), (11), (15))
`Calculate:` $\boldsymbol{F}, \boldsymbol{H}_i \rightarrow E_i$	Eqs. ((12), (16))

Computation of stress and tangent expressions

`Calculate:` $\psi_1, \psi_1', U, U', \psi_i, \psi_i'$	Eqs. ((17), (49))
`Calculate:` $\psi_1, U, \psi_i \rightarrow \boldsymbol{S}$	Eqs. ((19), (22), (24))
`Calculate:` $\psi_1', U', \psi_i' \rightarrow \mathbb{C}$	Eqs. ((28), (29), (32))

Return outputs

`Push Forward:` $\boldsymbol{S} \rightarrow \boldsymbol{\tau}$	Eqs. ((21), (22), (24))
`Push Forward:` $\mathbb{C} \rightarrow \mathbb{c}$	Eqs. ((28), (29), (32))

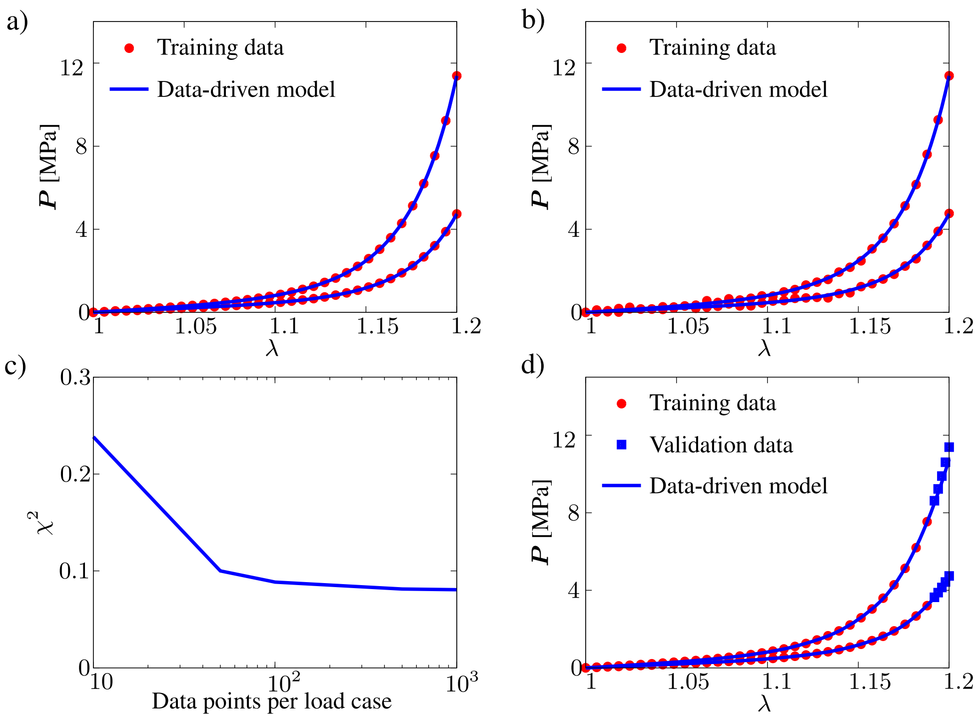

Fig. 9. (a) Predictions for ET dataset generated with an analytical model (Holzapfel et al., 2015), (b) predictions for the dataset polluted with Gaussian noise, (c) convergence of quality of fit as the number of training data points increases, (d) extrapolation ability of the data-driven model.

Cox-de Boor recursive function calls within the material subroutine. In this case, B-spline functions can be calculated directly in a single line, by writing out a closed form expression for a given polynomial degree.

5.1. Finite element example: Extension-inflation-torsion test of a hollow cylindrical tube

We conducted an extension-inflation-torsion simulation to demonstrate the performance of our model under extreme loading conditions. We used B-Spline model parameters corresponding to the biaxial testing data from Gültekin et al. (2016). Our study involved a hollow cylindrical tube with a geometry inspired by Gültekin et al. (2019), which represents a hypothetical tissue with a single layer containing two families of dispersed collagen fibers. These families have identical mechanical properties and are oriented at an average angle of $\theta = 45°$ relative to the cross-sectional plane, see Figs. 10c, 10d. The cylinder has an inner radius of 8 mm and a wall thickness of 2 mm. At the bottom face, the cylinder is fixed in the $\hat{u}_x$, $\hat{u}_y$, $\hat{u}_z$ directions. To apply loading to the cylinder, we twisted it by 60°, applied a displacement of $\hat{u}_z = 2$ mm at the top face, and exerted a pressure of 50 mmHg at the inner surface of the cylinder as shown in Fig. 10a. The displacement in the z-direction on the top face, the torsion on the top face, and the

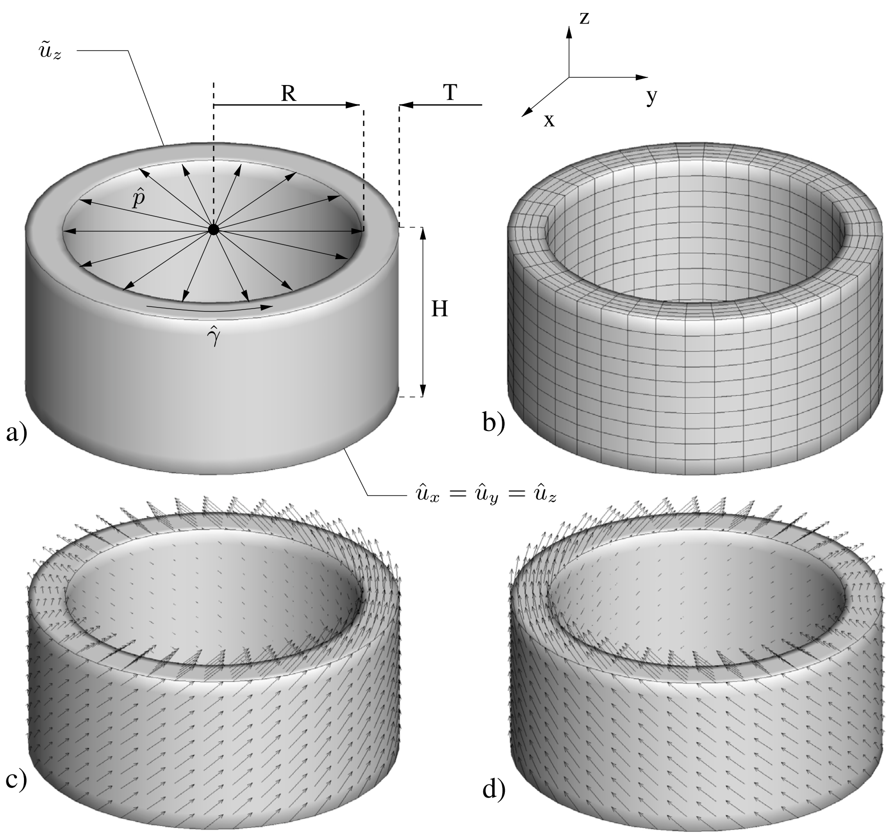

Fig. 10. (a) A hypothetical tissue piece of cylindrical geometry with dimensions H = 10, T = 2 , and R = 8 mm with boundary conditions $\hat{u}_x = \hat{u}_y = \hat{u}_z = 0$ mm, $\tilde{u}_z = 2$ mm, $\hat{\gamma} = 60°$ and $\hat{p} = 50$ mm Hg; (b) finite element mesh for the geometry; (c) visualization of mean directions of the first family of fibers $\boldsymbol{M}_1$; (d) visualization of mean directions of the second family of fibers $\boldsymbol{M}_2$ at each node.

Table 1
Rate of convergence of the global residual for the extension-inflation-torsion example. Convergence is attained at the third iteration in each of the given time steps.

Time [s]	0.25	0.50	0.75	1.00
Iteration 1	6.4004e+01	5.8199e+01	5.3896e+01	5.0006e+01
Iteration 2	8.7048e−02	9.5242e−02	5.5149e−02	8.7881e−02
Iteration 3	1.6292e−07	2.0535e−07	1.2190e−07	1.2465e−07

pressure load on the inner surface were all gradually increased in a linear manner. We discretized the tube into 2000 hexahedral elements with 5 elements in thickness, 40 elements in circumferential, and 10 elements in axial directions. Q1P0 elements are used throughout the simulation. The proposed model is highly robust and exhibits excellent convergence behavior, as shown in Table 1. The results of the finite element analysis are presented in Fig. 11, which displays the components of Cauchy stress in the radial, circumferential, and axial directions.

6. Concluding remarks

In conclusion, we have presented a data-driven anisotropic hyperelastic constitutive model that can capture the behavior of various biological tissues within the same constitutive framework. The proposed model uses B-Splines to substitute partial derivatives of the free energy function, making it flexible and able to adapt to varying mechanical characteristics of different tissues. The invariant-based formulation of the free energy function enables us to account for volumetric-isochoric deformation and dispersion characteristics of fiber families using generalized structure tensors. We have demonstrated the excellent fitting performance of the proposed model using an experimental dataset of four different biological tissues. The B-Spline-based structure of the model allows

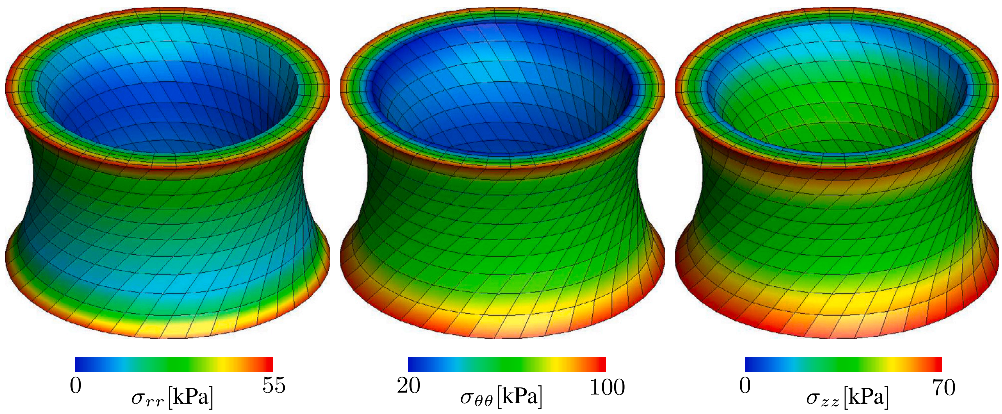

Fig. 11. Distributions of the radial σ_{rr}, the circumferential $\sigma_{\theta\theta}$, and the axial σ_{zz} Cauchy stress components at the end of the simulation.

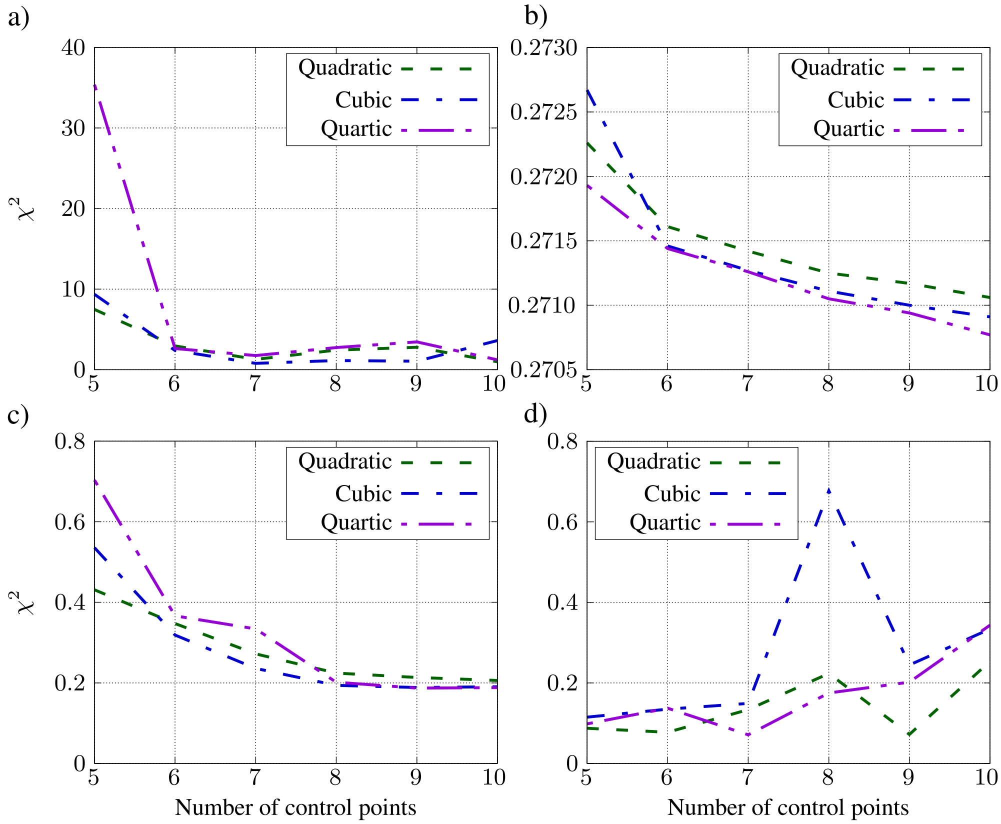

Fig. A.12. Sensitivity of the quality of fit metric to number of control points and quadratic, cubic, and quartic basis functions for (a) AAA, (b) myocardium, (c) linea alba, (d) rectus sheath tissues.

it to provide an accurate fit to each tissue despite their varying mechanical characteristics. Additionally, we have showcased the implementation of the model in finite element simulations and demonstrated the convergence under extreme loading conditions. In the proposed framework, the polyconvexity condition is applied during the training process. Polyconvexity is not a physical necessity; instead, it serves as a mathematical requirement that is not obligatory for all materials in a constitutive sense. Its principal importance lies in its role as a mathematical concept indicating strong ellipticity, which, in turn, assures the stability of materials. This stability is crucial for numerical applications such as finite element analysis. From a practical perspective, integrating polyconvexity is a more straightforward approach compared to directly implementing ellipticity. In this framework, we employ polyconvexity as a practical means to guarantee material stability and fulfill growth conditions. We believe that this new data-driven model will be useful for users who need good modeling capabilities without having expertise in a wide range of constitutive models and their intended

Table A.2
Optimized control points found for triaxial shearing tests of myocardium tissue (Sommer et al., 2015).

	Quadratic basis				Cubic basis				Quartic basis			
	Ψ_1	Ψ_f	Ψ_s	Ψ_{fs}	Ψ_1	Ψ_f	Ψ_s	Ψ_{fs}	Ψ_1	Ψ_f	Ψ_s	Ψ_{fs}
With 5 control points												
$\mathcal{P}_1$	0.2047	0.0000	0.0000	0.0000	0.2058	0.0000	0.0000	0.0000	0.2046	0.0000	0.0000	0.0000
$\mathcal{P}_2$	0.2432	0.1719	0.1816	0.0342	0.2450	0.1727	0.1821	0.0323	0.2617	0.1647	0.1936	0.0326
$\mathcal{P}_3$	0.3805	0.4169	0.2866	0.0436	0.3434	0.3331	0.2579	0.0556	0.3665	0.4119	0.2834	0.0327
$\mathcal{P}_4$	0.6933	1.0735	0.5544	0.0876	0.6786	1.0346	0.5287	0.0572	0.4756	0.5495	0.2958	0.0328
$\mathcal{P}_5$	1.0716	1.9602	1.0080	0.3842	1.0742	1.9671	1.0124	0.3905	1.0740	1.9689	1.0088	0.3397
With 8 control points												
$\mathcal{P}_1$	0.1994	0.0000	0.0000	0.0000	0.1981	0.0000	0.0000	0.0000	0.19753	0.0000	0.0000	0.0000
$\mathcal{P}_2$	0.2276	0.1756	0.1853	0.0203	0.2243	0.1751	0.1839	0.1815	0.2238	0.1750	0.1833	0.0179
$\mathcal{P}_3$	0.2757	0.2305	0.2051	0.0244	0.2569	0.2006	0.1933	0.0221	0.2529	0.1959	0.1920	0.0210
$\mathcal{P}_4$	0.3476	0.3549	0.2613	0.0257	0.3353	0.3282	0.2498	0.0234	0.3169	0.2863	0.2324	0.0225
$\mathcal{P}_5$	0.4556	0.5759	0.3491	0.0501	0.4623	0.5892	0.3547	0.0502	0.4690	0.6030	0.3605	0.0458
$\mathcal{P}_6$	0.6211	0.9265	0.4989	0.1001	0.6749	1.0406	0.5466	0.1154	0.6886	1.0677	0.5556	0.1213
$\mathcal{P}_7$	0.8738	1.4891	0.7633	0.1935	0.9107	1.5752	0.8078	0.2151	0.9201	1.5974	0.8202	0.2175
$\mathcal{P}_8$	1.0765	1.9765	1.0184	0.4150	1.0773	1.9789	1.0196	0.4214	1.0774	1.9794	1.0197	0.4237
With 10 control points												
$\mathcal{P}_1$	0.1970	0.0000	0.0000	0.0000	1.1952	0.0000	0.0000	0.0000	1.1942	0.0000	0.0000	0.0000
$\mathcal{P}_2$	0.2229	0.1752	0.1848	0.0157	0.2193	0.1733	0.1828	0.0133	0.2176	0.1722	0.1822	0.0123
$\mathcal{P}_3$	0.2559	0.2046	0.1848	0.0201	0.2521	0.1872	0.1897	0.0193	0.2374	0.1835	0.1884	0.0713
$\mathcal{P}_4$	0.3014	0.2737	0.2252	0.0201	0.2894	0.2524	0.2142	0.0193	0.2748	0.2271	0.2025	0.0184
$\mathcal{P}_5$	0.3605	0.3807	0.2715	0.0273	0.3536	0.3658	0.2667	0.0242	0.3439	0.3446	0.2589	0.0211
$\mathcal{P}_6$	0.4427	0.5499	0.3389	0.0487	0.4468	0.5584	0.3412	0.0500	0.4516	0.5685	0.3441	0.0574
$\mathcal{P}_7$	0.5543	0.7871	0.4377	0.0777	0.5790	0.8355	0.4602	0.0847	0.6128	0.9052	0.4905	0.0946
$\mathcal{P}_8$	0.7093	1.1209	0.5879	0.1305	0.7719	1.2591	0.6498	0.1507	0.8016	1.3268	0.6804	0.1593
$\mathcal{P}_9$	0.9225	1.6049	0.8240	0.2363	0.9570	1.6865	0.8678	0.2674	0.9714	1.7201	0.8866	0.2841
$\mathcal{P}_{10}$	1.0772	1.9785	1.0193	0.4205	1.0776	1.9799	1.0196	0.4235	1.0777	1.9805	1.0197	0.4238

applications. The model can be useful in digital twin applications and clinical patient-specific modeling studies where clinicians need a practical and flexible constitutive model. It eliminates the need for many carefully-picked models aimed at specific tissues appearing in simulations, making it a more efficient and practical choice. Overall, the proposed B-Spline model provides excellent fitting performance, ease of implementation. We hope that this model will contribute to further advancements in modeling biological tissues and aid in the development of patient-specific models for clinical applications.

CRediT authorship contribution statement

Oğuz Ziya Tikenoğulları: Validation, Software, Visualization, Investigation, Writing – original draft. **Alp Kağan Açan:** Validation, Software, Visualization, Investigation, Writing – original draft. **Ellen Kuhl:** Supervision, Writing – review & editing. **Hüsnü Dal:** Conceptualization, Methodology, Supervision, Writing – original draft, Funding acquisition.

Declaration of competing interest

The authors declare that they have no known competing financial interests or personal relationships that could have appeared to influence the work reported in this paper.

Data availability

Data will be made available on request.

Acknowledgments

This work was supported by Tübitak Bideb 2236 Co-funded Brain Circulation Scheme 2 (European Commission Horizon 2020 Marie Skłodowska-Curie Actions Cofund program) under the grant number 120C350.

Appendix. Optimized control point values and quality of fit

See Fig. A.12 and Tables A.2–A.5.

Table A.3
Optimized control points found for equibiaxial stretch tests of aneurysmatic abdominal aorta tissue (Niestrawska et al., 2016).

	Quadratic basis			Cubic basis			Quartic basis		
	ψ_1	ψ_4	ψ_6	ψ_1	ψ_4	ψ_6	ψ_1	ψ_4	ψ_6
With 5 control points									
$\mathcal{P}_1$	0.0000	0.0000	0.0000	0.0000	0.0000	0.0000	0.0000	0.0000	0.0000
$\mathcal{P}_2$	0.1868	0.2107	0.2107	0.0535	0.6457	0.6457	0.0022	0.0028	0.0028
$\mathcal{P}_3$	0.2964	1.2313	1.2313	0.0602	0.7471	0.7471	0.0034	0.0041	0.0041
$\mathcal{P}_4$	0.3175	1.3583	1.3583	0.0640	0.7551	0.7551	0.0051	0.0055	0.0055
$\mathcal{P}_5$	5.2909	22.424	22.424	5.8764	21.781	21.781	12.332	13.257	13.257
With 8 control points									
$\mathcal{P}_1$	0.0000	0.0000	0.0000	0.0000	0.0000	0.0000	0.0000	0.0000	0.0000
$\mathcal{P}_2$	0.3569	0.3051	0.3051	0.3164	0.2428	0.2428	0.3199	0.2921	0.2921
$\mathcal{P}_3$	0.5765	0.4864	0.4864	0.5098	0.3858	0.3858	0.5030	0.4615	0.4615
$\mathcal{P}_4$	0.8131	0.6820	0.6820	0.6956	0.5427	0.5427	0.6685	0.6289	0.6289
$\mathcal{P}_5$	1.0838	1.0234	1.0234	0.8702	0.8856	0.8856	0.8706	0.8835	0.8835
$\mathcal{P}_6$	1.3372	2.0668	2.0668	1.0674	2.7336	2.7336	1.2582	2.9613	2.9613
$\mathcal{P}_7$	1.5566	8.9471	8.9471	1.1582	10.749	10.749	1.8192	10.734	10.734
$\mathcal{P}_8$	3.6824	25.502	25.502	1.6702	27.483	27.483	2.8089	26.626	26.626
With 10 control points									
$\mathcal{P}_1$	0.0000	0.0000	0.0000	0.0000	0.0000	0.0000	0.0000	0.0000	0.0000
$\mathcal{P}_2$	0.3058	0.2094	0.2094	0.3337	0.2662	0.2662	0.2832	0.1998	0.1998
$\mathcal{P}_3$	0.4792	0.3323	0.3323	0.5212	0.4145	0.4145	0.4474	0.3124	0.3124
$\mathcal{P}_4$	0.6427	0.4490	0.4490	0.6893	0.5488	0.5488	0.6011	0.4165	0.4165
$\mathcal{P}_5$	0.8213	0.5927	0.5927	0.8732	0.7123	0.7123	0.7720	0.5482	0.5482
$\mathcal{P}_6$	0.9667	0.8642	0.8642	1.0787	0.9905	0.9905	0.9423	0.8439	0.8439
$\mathcal{P}_7$	1.0686	1.5804	1.5804	1.3108	1.7458	1.7458	1.0747	1.8955	1.8955
$\mathcal{P}_8$	1.1618	4.1155	4.1155	1.5924	5.3615	5.3615	1.1935	6.1095	6.1095
$\mathcal{P}_9$	1.2431	12.453	12.453	2.2257	14.367	14.367	1.4151	16.261	16.261
$\mathcal{P}_{10}$	1.6705	27.446	27.446	2.8943	26.549	26.549	1.7564	27.519	27.519

Table A.4
Optimized control points found for uniaxial stretch tests of linea alba tissue (Cooney et al., 2016).

	Quartic basis		Cubic basis		Quadratic basis	
	ψ_1	ψ_s	ψ_1	ψ_s	ψ_1	ψ_s
With 5 control points						
$\mathcal{P}_1$	0.0000	0.0000	0.0000	0.0000	0.0000	0.0000
$\mathcal{P}_2$	0.9281	0.3732	0.8743	0.3683	1.0435	0.5225
$\mathcal{P}_3$	0.9883	2.5971	0.9869	2.6236	1.0707	2.7741
$\mathcal{P}_4$	1.0615	4.5657	1.0800	4.6102	1.0935	4.1639
$\mathcal{P}_5$	1.1361	5.6701	1.1987	5.7158	1.1288	5.7230
With 8 control points						
$\mathcal{P}_1$	0.0000	0.0000	0.0000	0.0000	0.0000	0.0000
$\mathcal{P}_2$	0.7668	0.2459	0.7502	0.2799	0.7235	0.2526
$\mathcal{P}_3$	0.8804	0.8392	0.8680	0.4358	0.8495	0.3634
$\mathcal{P}_4$	0.9486	2.1115	0.9452	2.0330	0.9394	1.8891
$\mathcal{P}_5$	1.0053	2.9565	1.0112	3.0090	1.0070	3.1615
$\mathcal{P}_6$	1.0482	3.9611	1.0574	4.2825	1.0606	4.3405
$\mathcal{P}_7$	1.0918	5.1558	1.1017	5.2798	1.1137	5.3410
$\mathcal{P}_8$	1.1485	5.5977	1.1552	5.5963	1.1766	5.5894
With 10 control points						
$\mathcal{P}_1$	0.0000	0.0000	0.0000	0.0000	0.0000	0.0000
$\mathcal{P}_2$	0.6710	0.2511	0.6147	0.2312	0.6021	0.2603
$\mathcal{P}_3$	0.8193	0.5268	0.7840	0.3441	0.7737	0.2821
$\mathcal{P}_4$	0.8932	1.3612	0.8752	1.0965	0.8674	0.8037
$\mathcal{P}_5$	0.9491	2.1612	0.9411	2.1465	0.9415	2.0935
$\mathcal{P}_6$	0.9963	2.8481	0.9946	2.8817	0.9988	2.9732
$\mathcal{P}_7$	1.0346	3.5796	1.0385	3.7091	1.0441	3.8326
$\mathcal{P}_8$	1.0699	4.4118	1.0805	4.8042	1.0863	5.0240
$\mathcal{P}_9$	1.1093	5.3003	1.1269	5.3501	1.1322	5.3396
$\mathcal{P}_{10}$	1.1566	5.5976	1.1817	5.6032	1.1864	5.5866

Table A.5
Optimized control points found for uniaxial stretch tests of rectus sheath tissue (Martins et al., 2012).

	Quadratic basis		Cubic basis		Quartic basis	
	ψ_1	ψ_f	ψ_1	ψ_f	ψ_1	ψ_f
With 5 control points						
$\mathcal{P}_1$	0.0000	0.0000	0.0000	0.0000	0.0000	0.0000
$\mathcal{P}_2$	0.2082	0.0641	0.2154	0.0785	0.3257	0.0748
$\mathcal{P}_3$	0.5642	0.2436	0.5603	0.2119	0.5436	0.2073
$\mathcal{P}_4$	0.8007	1.1316	0.8256	0.9952	0.7579	0.7369
$\mathcal{P}_5$	0.9745	1.5190	0.9386	1.7472	0.9506	1.6421
With 8 control points						
$\mathcal{P}_1$	0.0000	0.0000	0.0000	0.0000	0.0000	0.0000
$\mathcal{P}_2$	0.1496	0.0850	0.1457	0.1276	0.1090	0.0636
$\mathcal{P}_3$	0.2803	0.1498	0.2578	0.2103	0.2201	0.1080
$\mathcal{P}_4$	0.4573	0.2690	0.4210	0.3229	0.4336	0.1986
$\mathcal{P}_5$	0.6046	0.5055	0.6074	0.5912	0.6359	0.5406
$\mathcal{P}_6$	0.7505	0.8772	0.7880	0.9492	0.8415	0.9168
$\mathcal{P}_7$	0.9299	1.1694	0.9428	0.2358	1.0175	1.1176
$\mathcal{P}_8$	1.0159	1.8085	1.0498	1.9697	1.0828	1.7153
With 10 control points						
$\mathcal{P}_1$	0.0000	0.0000	0.0000	0.0000	0.0000	0.0000
$\mathcal{P}_2$	0.1181	0.0854	0.1168	0.0801	0.1029	0.0779
$\mathcal{P}_3$	0.2124	0.1355	0.1992	0.1273	0.1753	0.1240
$\mathcal{P}_4$	0.3449	0.2028	0.3121	0.1856	0.2763	0.1783
$\mathcal{P}_5$	0.4815	0.3114	0.4633	0.2949	0.4391	0.2759
$\mathcal{P}_6$	0.5944	0.4753	0.5918	0.4877	0.6099	0.5037
$\mathcal{P}_7$	0.6937	0.7329	0.7238	0.7735	0.7743	0.8068
$\mathcal{P}_8$	0.8232	1.0139	0.9022	1.0151	0.9235	1.0253
$\mathcal{P}_9$	0.9328	1.2427	1.0032	1.2150	1.0052	1.2498
$\mathcal{P}_{10}$	0.9877	2.3343	1.0600	2.3633	1.0605	2.4047

References

Alastrué, V., Martinez, M., Doblaré, M., Menzel, A., 2009. Anisotropic micro-sphere-based finite elasticity applied to blood vessel modelling. J. Mech. Phys. Solids 57, 178–203.

Alastrué, V., Sáez, P., Martínez, M., Doblaré, M., 2010. On the use of the bingham statistical distribution in microsphere-based constitutive models for arterial tissue. Mech. Res. Commun. 37, 700–706.

Ateshian, G.A., Rajan, V., Chahine, N.O., Canal, C.E., Hung, C.T., 2009. Modeling the matrix of articular cartilage using a continuous fiber angular distribution predicts many observed phenomena. J. Biomech. Eng. 131, 061003.

Ball, J.M., 1976. Convexity conditions and existence theorems in nonlinear elasticity. Arch. Ration. Mech. Anal. 63, 337–403.

Balzani, D., Neff, P., Schröder, J., Holzapfel, G.A., 2006. A polyconvex framework for soft biological tissues, adjustment to experimental data. Int. J. Solids Struct. 43, 6052–6070.

Bhattarai, A., Kowalczyk, W., Tran, T.N., 2021. A literature review on large intestinal hyperelastic constitutive modeling. Clin. Biomech. 105445.

Billiar, K.L., Sacks, M.S., 2000. Biaxial mechanical properties of the natural and glutaraldehyde treated aortic valve cusp-part i: Experimental results. J. Biomech. Eng. 122, 23–30.

Chagnon, G., Rebouah, M., Favier, D., 2015. Hyperelastic energy densities for soft biological tissues: A review. J. Elast. 120, 129–160.

Chuong, C., Fung, Y., 1983. Three-dimensional stress distribution in arteries. J. Biomech. Eng. 105, 268–274.

Ciarlet, P.G., 1988. Three-Dimensional Elasticity. Elsevier.

Conti, S., Müller, S., Ortiz, M., 2020. Data-driven finite elasticity. Arch., Ration. Mech. Anal. 237, 1–33.

Cooney, G.M., Lake, S.P., Thompson, D.M., Castile, R.M., Winter, D.C., Simms, C.K., 2016. Uniaxial and biaxial tensile stress-stretch response of human linea alba. J. Mech. Behav. Biomed. Mater. 63, 134–140.

Dal, H., Açan, C., Hossain, M., 2023a. An in silico-based investigation on anisotropic hyperelastic constitutive models for soft biological tissues. Arch. Comput. Methods Eng. 30, 4601–4632.

Dal, H., Denli, F., Açan, A., Kaliske, M., 2023b. Data-driven hyperelasticity – part I: A canonical isotropic formulation for rubberlike materials. J. Mech. Phys. Solids 179, 105381.

Davis, P.J., 1975. Interpolation and Approximation. Courier Corporation.

Dokos, S., Smaill, B.H., Young, A.A., LeGrice, I.J., 2002. Shear properties of passive ventricular myocardium. Am. J. Physiol.-Heart Circ. Physiol. 283, H2650–H2659.

Driessen, N.J., Bouten, C.V., Baaijens, F.P., 2005. A structural constitutive model for collagenous cardiovascular tissues incorporating the angular fiber distribution. J. Biomech. Eng. 127, 494–503.

Eggersmann, R., Kirchdoerfer, T., Reese, S., Stainier, L., Ortiz, M., 2019. Model-free data-driven inelasticity. Comput. Methods Appl. Mech. Eng. 350, 81–99.

Eriksson, T.S., Prassl, A.J., Plank, G., Holzapfel, G.A., 2013. Modeling the dispersion in electromechanically coupled myocardium. Int. J. Numer. Methods Biomed. Eng. 29, 1267–1284.

Fung, Y.C., 1993. Biomechanics: Mechanical Properties of Living Tissues. Springer, New York.

Fung, Y., Fronek, K., Patitucci, P., 1979. Pseudoelasticity of arteries and the choice of its mathematical expression. Am. J. Physiol.-Heart Cir. Physiol. 237, H620–H631.

Gasser, T.C., Ogden, R.W., Holzapfel, G.A., 2006. Hyperelastic modelling of arterial layers with distributed collagen fibre orientations. J. R. Soc. Interface 3, 15–35.

Ghaboussi, J., Garret, Jr., J., Wu, X., 1991. Knowledge-based modeling of material behavior with neural networks. J. Eng. Mech. 117, 132–153.

Ghaemi, H., Behdinan, K., Spence, A., 2009. In vitro technique in estimation of passive mechanical properties of bovine heart: Part i. Experimental techniques and data. Med. Eng. Phys. 31, 76–82.
Göktepe, S., 2007. Micro-Macro Approaches to Rubbery and Glassy Polymers: Predictive Micromechanically-Based Models and Simulations (Ph.D. thesis). Universität Stuttgart.
Gültekin, O., Dal, H., Holzapfel, G.A., 2019. On the quasi-incompressible finite element analysis of anisotropic hyperelastic materials. Comput. Mech. 63, 443–453.
Gültekin, O., Sommer, G., Holzapfel, G.A., 2016. An orthotropic viscoelastic model for the passive myocardium: Continuum basis and numerical treatment. Comput. Methods Biomech. Biomed. Eng. 19, 1647–1664.
Hashash, Y., Jung, S., Ghaboussi, J., 2004. Numerical implementation of a neural network based material model in finite element analysis. Int. J. Numer. Methods Eng. 59, 989–1005.
Holzapfel, G.A., 2000. Nonlinear Solid Mechanics: A Continuum Approach for Engineering. Johnn Wiley & Sons, Chichester.
Holzapfel, G.A., Gasser, T.C., Ogden, R.W., 2000. A new constitutive framework for arterial wall mechanics and a comparative study of material models. J. Elasticity Phys. Sci. Solids 61, 1–48.
Holzapfel, G.A., Niestrawska, J.A., Ogden, R.W., Reinisch, A.J., Schriefl, A.J., 2015. Modelling non-symmetric collagen fibre dispersion in arterial walls. J. R. Soc. Interface 12, 20150188.
Holzapfel, G.A., Ogden, R.W., Sherifova, S., 2019. On fibre dispersion modelling of soft biological tissues: A review. Proc. R. Soc. A 475, 20180736.
Holzapfel, G.A., Sommer, G., Gasser, C.T., Regitnig, P., 2005. Determination of layer-specific mechanical properties of human coronary arteries with nonatherosclerotic intimal thickening and related constitutive modeling. Am. J. Physiol.-Heart Circ. Physiol. 289, H2048–H2058.
Horgan, C.O., Saccomandi, G., 2005. A new constitutive theory for fiber-reinforced incompressible nonlinearly elastic solids. J. Mech. Phys. Solids 53, 1985–2015.
Humphrey, J.D., 1995. Mechanics of the arterial wall: Review and directions. Crit. Rev. Biomed. Eng. 23, 1–162.
Humphrey, J.D., 2002. Cardiovascular Solid Mechanics: Cells, Tissues, and Organs. Springer, New York.
Humphrey, J.D., Strumpf, R.K., Yin, F.C.P., 1990. Determination of a constitutive relation for passive myocardium: I. A new functional form. J. Biomech. Eng. 112, 333–339.
Ibanez, R., Abisset-Chavanne, E., Aguado, J.V., Gonzalez, D., Cueto, E., Chinesta, F., 2018. A manifold learning approach to data-driven computational elasticity and inelasticity. Arch. Comput. Methods Eng. 25, 47–57.
Ibanez, R., Borzacchiello, D., Aguado, J.V., Abisset-Chavanne, E., Cueto, E., Ladeveze, P., Chinesta, F., 2017. Data-driven non-linear elasticity: Constitutive manifold construction and problem discretization. Comput. Mech. 60, 813–826.
Kalra, A., Lowe, A., Al-Jumaily, A., 2016. Mechanical behaviour of skin: A review. J. Mater. Sci. Eng. 5, 1000254.
Kanno, Y., 2018a. Data-driven computing in elasticity via kernel regression. Theor. Appl. Mech. Lett. 8, 361–365.
Kanno, Y., 2018b. Simple heuristic for data-driven computational elasticity with material data involving noise and outliers: A local robust regression approach. Japan J. Ind. Appl. Math. 35, 1085–1101.
Karlon, W.J., Covell, J.W., Mcculloch, A.D., Hunter, J.J., Omens, J.H., 1998. Automated measurement of myofiber disarray in transgenic mice with ventricular expression of ras. Anat. Rec.: Off. Publ. Am. Assoc. Anatomists 252, 612–625.
Kirchdoerfer, T., Ortiz, M., 2016. Data-driven computational mechanics. Comput. Methods Appl. Mech. Eng. 304, 81–101.
Kirchdoerfer, T., Ortiz, M., 2018. Data-driven computing in dynamics. Int. J. Numer. Methods Eng. 113, 1697–1710.
Lanir, Y., 1979. A structural theory for the homogeneous biaxial stress-strain relationships in flat collagenous tissues. J. Biomech. 12, 423–436.
Latorre, M., Montáns, F.J., 2013. Extension of the sussman–bathe spline-based hyperelastic model to incompressible transversely isotropic materials. Comput. Struct. 122, 13–26.
Latorre, M., Montáns, F.J., 2014. What-you-prescribe-is-what-you-get orthotropic hyperelasticity. Comput. Mech. 53, 1279–1298.
Lefik, M., Schrefler, B.A., 2003. Artificial neural network as an incremental non-linear constitutive model for a finite element code. Comput. Methods Appl. Mech. Eng. 192, 3265–3283.
Linka, K., Hillgärtner, M., Abdolazizi, K.P., Aydin, R.C., Itskov, M., Cyron, C.J., 2021. Constitutive artificial neural networks: A fast and general approach to predictive data-driven constitutive modeling by deep learning. J. Comput. Phys. 429, 110010.
Linka, K., Kuhl, E., 2023. A new family of constitutive artificial neural networks towards automated model discovery. Comput. Methods Appl. Mech. Eng. 403, 115731.
Martins, P., Peña, E., Jorge, R.N., Santos, A., Santos, L., Mascarenhas, T., Calvo, B., 2012. Mechanical characterization and constitutive modelling of the damage process in rectus sheath. J. Mech. Behav. Biomed. Mater. 8, 111–122.
May-Newman, K., Yin, F., 1998. A constitutive law for mitral valve tissue. J. Biomech. Eng. 120, 38–47.
Mihai, L.A., Chin, L., Janmey, P.A., Goriely, A., 2015. A comparison of hyperelastic constitutive models applicable to brain and fat tissues. J. R. Soc. Interface 12, 20150486.
Murphy, J., 2013. Transversely isotropic biological, soft tissue must be modelled using both anisotropic invariants. Eur. J. Mech.-A/Solids 42, 90–96.
Nguyen, L.T.K., Aydin, R.C., Cyron, C.J., 2022. Accelerating the distance-minimizing method for data-driven elasticity with adaptive hyperparameters. Comput. Mech. 70, 621–638.
Nguyen, L.T.K., Keip, M.-A., 2018. A data-driven approach to nonlinear elasticity. Comput. Struct. 194, 97–115.
Nguyen, L.T.K., Rambausek, M., Keip, M.-A., 2020. Variational framework for distance-minimizing method in data-driven computational mechanics. Comput. Methods Appl. Mech. Eng. 365, 112898.
Niestrawska, J.A., Viertler, C., Regitnig, P., Cohnert, T.U., Sommer, G., Holzapfel, G.A., 2016. Microstructure and mechanics of healthy and aneurysmatic abdominal aortas: Experimental analysis and modelling. J. R. Soc. Interface 13, 20160620.
Ogden, R.W., Saccomandi, G., 2007. Introducing mesoscopic information into constitutive equations for arterial walls. Biomech. Model. Mechanobiol. 6, 333–344.
Platzer, A., Leygue, A., Stainier, L., 2019. Assessment of data-driven computational mechanics in finite strain elasticity. In: Constitutive Models for Rubber XI. CRC Press, pp. 230–236.
Sacks, M.S., 2003. Incorporation of experimentally-derived fiber orientation into a structural constitutive model for planar collagenous tissues. J. Biomech. Eng. 125, 280–287.
Schriefl, A.J., Collins, M.J., Pierce, D., Holzapfel, G.A., Niklason, L.E., Humphrey, J.D., 2012a. Remodeling of intramural thrombus and collagen in an ang-ii infusion apoe-/- model of dissecting aortic aneurysms. Thrombosis Res. 130, e139–e146.
Schriefl, A.J., Reinisch, A.J., Sankaran, S., Pierce, D.M., Holzapfel, G.A., 2012b. Quantitative assessment of collagen fibre orientations from two-dimensional images of soft biological tissues. J. R. Soc. Interface 9, 3081–3093.
Schriefl, A.J., Wolinski, H., Regitnig, P., Kohlwein, S.D., Holzapfel, G.A., 2013. An automated approach for three-dimensional quantification of fibrillar structures in optically cleared soft biological tissues. J. R. Soc. Interface 10, 20120760.
Schriefl, A.J., Zeindlinger, G., Pierce, D.M., Regitnig, P., Holzapfel, G.A., 2012c. Determination of the layer-specific distributed collagen fibre orientations in human thoracic and abdominal aortas and common iliac arteries. J. R. Soc. Interface 9, 1275–1286.
Schröder, J., Neff, P., 2003. Invariant formulation of hyperelastic transverse isotropy based on polyconvex free energy functions. Int. J. Solids Struct. 40, 401–445.
Sommer, G., Schriefl, A.J., Andrä, M., Sacherer, M., Viertler, C., Wolinski, H., Holzapfel, G.A., 2015. Biomechanical properties and microstructure of human ventricular myocardium. Acta Biomater. 24, 172–192.

Strijkers, G.J., Bouts, A., Blankesteijn, W.M., Peeters, T.H., Vilanova, A., van Prooijen, M.C., Sanders, H.M., Heijman, E., Nicolay, K., 2009. Diffusion tensor imaging of left ventricular remodeling in response to myocardial infarction in the mouse. NMR in Biomed.: Int. J. Devoted Dev. Appl. Magn. Reson. vivo 22, 182–190.

Sussman, T., Bathe, K.-J., 2009. A model of incompressible isotropic hyperelastic material behavior using spline interpolations of tension–compression test data. Commun. Numer. Methods Eng. 25, 53–63.

Tac, V., Sree, V.D., Rausch, M.K., Tepole, A.B., 2022. Data-driven modeling of the mechanical behavior of anisotropic soft biological tissue. Eng. Comput. 38, 4167–4182.

Taylor, R.L., 2014. FEAP - finite element analysis program. URL http://www.ce.berkeley/feap.

Tong, P., Fung, Y.-C., 1976. The stress-strain relationship for the skin. J. Biomech. 9, 649–657.

Usyk, T., Omens, J., McCulloch, A., 2001. Regional septal dysfunction in a three-dimensional computational model of focal myofiber disarray. Am. J. Physiol.-Heart Circ. Physiol. 281, H506–H514.

Weiss, J.A., Maker, B.N., Govindjee, S., 1996. Finite element implementation of incompressible, transversely isotropic hyperelasticity. Comput. Methods Appl. Mech. Eng. 135, 107–128.

Xu, K., Huang, D.Z., Darve, E., 2021. Learning constitutive relations using symmetric positive definite neural networks. J. Comput. Phys. 428, 110072.

Zulliger, M.A., Fridez, P., Hayashi, K., Stergiopulos, N., 2004. A strain energy function for arteries accounting for wall composition and structure. J. Biomech. 37, 989–1000.